ADVANCED FUNCTIONAL MATERIALS
www.afm-journal.de

Additive Manufacturing with Cellulose-Based Composites: Materials, Modeling, and Applications

Shuvodeep De, Shalini J. Rukmani, Xianhui Zhao, Caitlyn Clarkson, Frederic Vautard, Samarthya Bhagia, Monojoy Goswami, Shuyang Zhang, Sana F. Elyas, Wei Zhao, Jeremy C. Smith, Arthur J. Ragauskas, Soydan Ozcan, Halil Tekinalp,* Muqing Si, Jinrui Huang, and Ximin He**

Recent advances in large-scale additive manufacturing (AM) with polymer-based composites have enabled efficient production of high-performance materials. Cellulose nanomaterials (CNMs) have emerged as bio-based feedstocks due to their exceptional strength and sustainability. However, challenges such as hornification and poor dispersion in polymer matrices still limit large-scale CNM–polymer composite manufacturing, requiring novel strategies. This review outlines an approach starting with atomic-level simulations to link molecular composition to key parameters like bulk density, viscosity, and modulus. These simulations provide data for finite element analysis (FEA), which informs large-scale experiments and reduces the need for extensive trials. The strategy explores how atomic interactions impact the morphology, adhesion, and mechanical properties of CNM-based composites in AM processes. The review also discusses current developments in AM, along with predictions of mechanical and thermal properties for structural applications, packaging, flexible electronics, and hydrogel scaffolds. By integrating experimental findings with molecular dynamics (MD) simulations and finite element modeling (FEM), valuable insights for material design, process optimization, and performance enhancement in CNM-based AM are provided to address ongoing challenges.

1. Introduction

AM, known colloquially as 3D printing, is a computer-aided suite of techniques in which items are fabricated by filling materials in a 3D design space, usually layer by layer.[1] AM technology has developed rapidly in recent years because of the speed, reduction in process waste, reduction in energy consumption, and low cost that it offers.[2,3] AM can be used with metals, ceramics, polymers, and polymer-based composites.[4,5] The technique mainly employs fused filament fabrication/melt extrusion deposition, digital light processing, and direct ink writing.[6] For polymer-based AM approaches, extrusion-based large-scale AM is ≈200 times faster than conventional desktop 3D printing.

AM has the advantage of enabling the production of complex geometries without the need for special jigs, devices, or tools.[7] However, many process variables (e.g.,

S. De, J. C. Smith
Computing and Computational Sciences Directorate
Oak Ridge National Laboratory
Oak Ridge, TN 37830, USA

S. J. Rukmani, J. C. Smith
UT/ORNL Center for Molecular Biophysics
Oak Ridge National Laboratory
Oak Ridge, TN 37831, USA

S. J. Rukmani, A. J. Ragauskas
Biochemistry and Cellular and Molecular Biology
University of Tennessee
Knoxville, TN 37996, USA

X. Zhao
Environmental Sciences Division
Oak Ridge National Laboratory
Oak Ridge, TN 37830, USA
E-mail: zhaox@ornl.gov

C. Clarkson, S. F. Elyas, S. Ozcan, H. Tekinalp
Manufacturing Science Division
Oak Ridge National Laboratory
Oak Ridge, TN 37830, USA
E-mail: tekinalphl@ornl.gov

F. Vautard, M. Goswami
Chemical Sciences Division
Oak Ridge National Laboratory
Oak Ridge, TN 37830, USA

S. Bhagia, A. J. Ragauskas
Biosciences Division
Oak Ridge National Laboratory
Oak Ridge, TN 37830, USA

S. Zhang
Chemical and Biomolecular Engineering
University of Tennessee
Knoxville, TN 37996, USA

The ORCID identification number(s) for the author(s) of this article can be found under https://doi.org/10.1002/adfm.202414222

DOI: 10.1002/adfm.202414222

temperature, speed, nozzle size, layer height, wall thickness) must be optimized. A particular challenge for the AM process is the control of the resolution and the microstructure. For polymer-based composites in particular, adhesion between the deposited layers is pivotal in determining their mechanical strength and integrity under service performance where the material is subjected to different types of loading.

There has been a growing need to develop sustainable solutions for large-scale and high-performance applications such as housing and construction, aerospace, and structural units such as bridges to provide carbon-neutral alternatives that minimize health, environment, and safety risks. A largely untapped market has consequently appeared for AM with bio-based polymers or composites.[2] Of particular interest in this regard is cellulose, the world's most abundant biopolymer, which can be derived from plant-based lignocellulosic biomass and possesses remarkable mechanical properties.[8] Cellulose has a complex hierarchical structure with different levels of organization across length scales ranging from sub-nanometer to several millimeters, while CNM specifically have at least one dimension on the order of nanometers. CNMs can be used effectively to enhance the mechanical performance of polymer resins as fillers compared to other reinforcing nanomaterials—including carbon nanotubes, ceramic nanoparticles, and metal nanoparticles—and, moreover, are non-toxic, biodegradable, renewable, and less energy-intensive during production.[9]

CNMs can be broadly classified into cellulose nanofibers (CNFs) and cellulose nanocrystals (CNCs, also known as nanowhiskers). CNFs and CNCs have a high elastic modulus along the fiber axis comparable to that of traditional reinforcing materials such as glass fibers and Kevlar.[10–12] Moreover, their specific modulus (i.e., the modulus to density ratio) is higher (65 J g^{-1} for nanocellulose) than that of structural reinforcing materials such as steel (25 J g^{-1}), making them attractive for light-weight structural applications.[13–15] The morphologies, high aspect ratios, and excellent mechanical properties of CNMs make them highly suitable as reinforcing materials for high-performance composite applications using a large-scale manufacturing technique such as AM. Other properties that make CNMs suitable for high-performance applications include their large specific surface area, high thermal resistance, the abundance of hydroxyl groups suitable to form composites with chemical bonding, and cost, as they can be sourced easily from plant biomass.[16–20] Recently, researchers produced CNFs from biomass feedstocks (such as plants and algae) by grinding the materials and removing hemicellulose and lignin, from food waste, and from old corrugated containers such as recycled cardboard.[17,21,22]

W. Zhao
School of Mechanical and Aerospace Engineering
Oklahoma State University
Stillwater, OK 74078, USA
M. Si, J. Huang, X. He
Material Science and Engineering
University of California
Los Angeles, CA 90095, USA
E-mail: ximinhe@ucla.edu

CNM–polymer composites have been manufactured, including CNM–polypropylene, CNM–polylactic acid (PLA), and CNM–high-density polyethylene (HDPE).[21,23] However, there are several challenges involved in both the material design and processing of CNM-based nanocomposites. Due to their hydrophilic nature, CNFs are typically found solvated in water that needs to be removed (i.e., dewatering) prior to melt-mixing CNF with polymers to make composite materials. Unfortunately, the removal of water causes irreversible aggregation of CNMs, called hornification, which results in them being transported as dilute solutions, thereby significantly increasing the transportation costs of bulk materials. Another challenge is an incompatibility of the hydrophilic CNF with mostly hydrophobic common polymer resins and thermoplastics such as PLA, PP, and polyethylene terephthalate glycol (PETG). This incompatibility leads to poor distribution of CNMs in the composite leading to weak interfaces, which further affect the matrix-filler load transfer and act as points of failure. The hydrophilic surfaces of CNMs further result in the aggregation of cellulose nanoparticles (CNPs) in polymer resins, which results in a decrease in mechanical strength.[18] While the above challenges are predominantly associated with material design on a microscopic level, the macroscopic rheological behavior of CNM-based nanocomposites influences the 3D printing process and service performance of these materials significantly, requiring optimization of both process parameters and evaluating bulk properties rigorously. Viscosity, shear thinning behavior, gelation, fluid flow, CNM fiber alignment, and entanglement effects of cellulose and polymer chains, affect the efficacy of extrusion and deposition during 3D printing.

Several solutions have been proposed and developed over the years to overcome different facets of these challenges, including better drying methods, improved fibrillation techniques, use of co-solvents/binders/additives/chemically modified CNMs, advancements in AM processes to incorporate 3D printing of CNM-based materials.[22,24,25] Computational studies have helped both to deepen the understanding of these challenges on a molecular scale and provided design and optimization of specific CNM-based materials. However, informed modeling spanning multiple techniques and length scales using both high-performance computing and previously available literature data can reduce the otherwise laborious experimental trial and error to optimize nanocomposite properties and 3D printing process parameters. On this front, previous review articles have focused on presenting individual advancements in material design and manufacturing of pure CNM and CNM-based nanocomposites. However, to our knowledge, no review article has put together key findings from the state-of-the-art and advancing 3D printing experimental techniques for CNMs and computational modeling approaches that address some of the challenges common to manufacturing of CNM nanocomposites that apply to 3D printing. Further, our review gives a perspective of how a synergistic experimental-modeling approach can both drive and augment the design and manufacturing of CNM-based nanocomposites on pilot-to-large-scales.

The article begins by introducing the CNM molecular structure and hierarchical organization in solid-state and in solution, water organization, CNM-solvent, and CNM-polymer interfacial properties obtained from experiments. We then delve into modeling techniques at multiple lengths and time scales

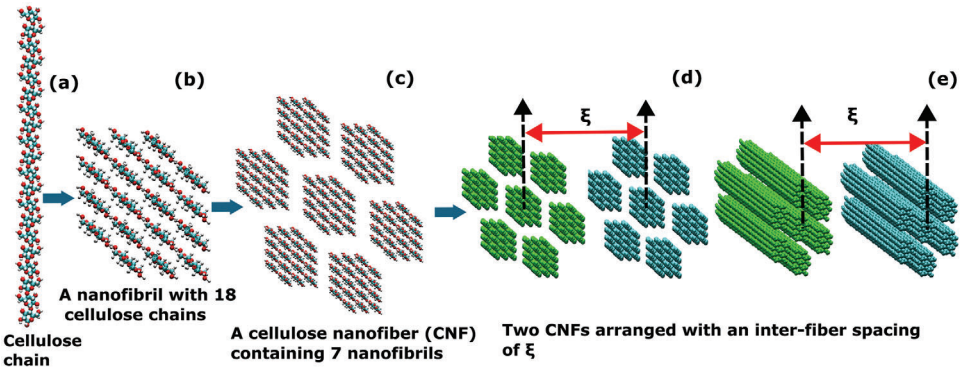

Figure 1. Cellulose organization at multiple levels showing a) a single polysaccharide cellulose chain with DP = 20, b) an 18-chain fibril, c) A CNF composed of 7 fibrils packed in a hexagonal arrangement with an initial inter-fibril spacing of 11 Å, d) and e) 2 CNFs with an inter-fiber spacing of ξ.

that provide an understanding of both materials design and process optimization: 1) MD simulations outlining fundamental CNM-solvent/CNM-polymer interactions, and strategies to improve nanocomposite properties such as CNM surface modifications, drying, and the use of co-solvents 2) FEM focusing on the optimization of parameters for 3D printing of these composites and evaluating their mechanical behavior. A proposed method is then provided for integrating experiments and various modeling approaches to devise a future strategy where synergistic modeling and experimental methods can be used successfully to 3D print CNM-based nanocomposites. We finally discuss relevant applications where 3D printed CNM-based nanocomposites have delivered a promising performance, such as high-strength structures such as buildings and bridges, advanced food packaging, flexible electronics, innovative microfluidic devices, and hydrogel scaffolds for biomedicine where our design principles can be applied. Our conclusions summarize the key findings from the literature and our original research, offering a forward-looking perspective on future trends in the design and manufacturing of AM for CNM-based materials. This review will serve as a useful resource for research in CNM-based nanomaterial design and nanotechnology process advances in additive manufacturing.

2. Molecular Structure and Properties of CNMs in Solid State and Solution

2.1. Hierarchical CNM Organization and Associated Molecular Interactions

Cellulose is a semicrystalline polymer with regions of high crystallinity separated by amorphous regions. It exists in different polymorphs, I, II, and III,[26,27] among which Iβ is the most commonly used in biofuels and nanocomposites because higher plants are rich in Iβ fraction relative to Iα.[16,26,27] Cellulose chains contain β(1,4) linked D-glucose monomers (**Figure 1A**) as repeating units, and several individual cellulose chains together make up a microfibril or a nanofibril. The terms "microfibril" and "nanofibril" have been (confusingly) interchangeably used over the years by researchers. The term "microfibril" has been used historically to indicate the basic unit that can be isolated from the cell wall and does not reflect the actual length scale of these fibrils, which are ≈3 nm in diameter and several micrometers in length. In the sections below, we call this basic unit a nanofibril. A nanofibril composed of 36 cellulose chains was commonly considered to be the fundamental unit in plant cell walls,[28] but in recent years, experimental, and modeling studies have shown evidence that the nanofibril exists as an 18-chain unit rather than one of 36, as shown in Figure 1B.[29,30] Nevertheless, nanofibrils with 18, 36, or 24 chains have been used in studies by researchers. Both CNFs and CNCs contain several nanofibrils that are bundled together: Figure 1C shows an atomistic MD simulation model (which is discussed in-depth later in this article) of a bundle composed of seven nanofibrils. CNCs have needle-like morphologies as a result of the removal of amorphous fragments via acid hydrolysis, and they have dimensions of 5–20 nm in diameter and 100–600 nm in length. CNFs, on the other hand, present a flexible, fiber-like structure with a diameter of 5–200 nm and lengths > 1 µm, consisting of both crystalline and amorphous regions. The morphologies and dimensions of CNFs are highly dependent on the extent of fibrillation and pretreatment strategies. In the literature, CNFs and CNCs are roughly demarcated by an aspect ratio (l/d) cutoff of 50, where CNFs have aspect ratios ≥50 and CNCs have aspect ratios <50.

Cellulose displays complex interactions, including hydrogen bonding, electrostatic, and van der Waals effects, at its various levels of organization. The glucan monomers in cellulose chains contain hydroxyl groups that are equatorially positioned and can form several intra-chain and inter-chain hydrogen bonds (shown in **Figure 2**), including bonds between the C3 hydroxyl group and the ring oxygen (O3-H···O5) and between the OH groups on C2 and C6 (O2H2···O6 or O6H6···O2). Although hydrogen bonding interactions are important in cellulose, their importance in explaining physical and mechanical properties has perhaps been overstated in the literature. For example, vibrational spectroscopy and quantum chemical density functional theory (DFT) simulations have shown that London dispersion (attractive van der Waals) forces contribute 50–70% of the total cohesive interaction in cellulose,[31] playing a major role in, for example, its high axial stiffness, insolubility in water, and anisotropy in thermal and mechanical properties.

The elastic modulus of highly crystalline cellulose along the axial direction (i.e., along the fiber axis) was found to be 134 GPa,[33,34] whereas for fibers derived from wood, the elastic modulus is lower, roughly between 20–50 GPa,[8,32] probably due to

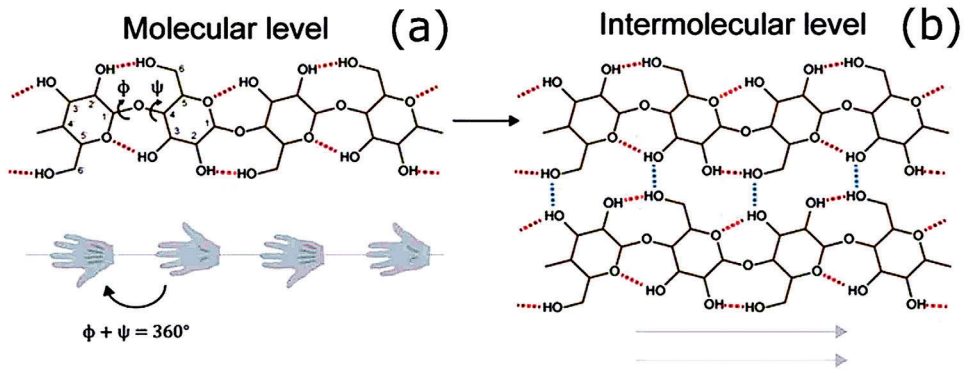

Figure 2. Structure of cellulose showing a) intrachain and b) interchain hydrogen bonding between the hydroxyl groups present on glucan units. The O5'-C1'-O4-C4 (φ) and C1'-O4-C4-C3 (ψ) dihedral angles are also shown in (a) for the reader to visualize how the change in conformations can change the intrachain hydrogen bonds. Adapted under the terms of the CC-BY-4.0 license.[32] Copyright 2021, Springer Nature.

the presence of amorphous regions and defects. The change in crystallinity and dimensions plays a role in determining moduli. For example, the use of polyethylene oxide (PEO)–reinforced composites with CNC fillers was found to result in higher Young's modulus than CNF fillers for the same reinforcement percentage.[35] This can be attributed to the CNFs containing both crystalline and amorphous regions (the degree of crystallinity can vary according to pretreatment and fibrillation method), whereas CNCs contain only crystalline segments. Both CNCs and highly crystalline CNFs along the axis modulus show comparable or superior mechanical strength (elastic modulus ≈150 GPa) to that of other reinforcing materials in composites such as Kevlar (≈110 GPa) and steel (200 GPa).[10–12] MD simulation studies determined that even though removing the intramolecular hydrogen bonds in cellulose reduced its modulus by 15–20%, a major contribution also came from covalent bonds, angle, and dihedral components, and, again, strong dispersion interactions.[36,37] Cooperative hydrogen bonding schemes along the glucan chains have also been proposed from neutron scattering, and this could be a further factor in strengthening axial intramolecular interactions and increasing the elastic modulus in the axial direction. The modulus of cellulose in the transverse direction is lower than it is in the axial direction, and non-covalent interactions are more important in this direction; DFT studies have shown increased dispersion interaction contributions in the transverse direction.[38] It is also important to note here that several of these interactions are interdependent, and it is non-trivial to theoretically isolate the effects of inter-chain hydrogen bonds and modify them, as changing hydrogen bond donors or acceptors in the cellulose chains influences other parameters such as chain stacking and charge distribution, thereby influencing the relative magnitudes of interaction types.

2.2. Water Organization around CNMs

Aggregation (also called agglomeration or hornification) has often been thought to be caused by irreversible hydrogen bond formation between fibers on the surface, although it was originally coined to define the decrease in water retention value (WRV) relative to the original value.[39,40] Aggregation includes both physical and chemical changes that occur during drying—including shrinkage and closure of voids—and structural reorganization caused by various forces, including long-range capillary forces, hydrogen bond formation, and dispersion forces. In this regard, water organization around CNMs has been the subject of extensive study by various experimental and computational researchers.[32,37,41–45] The types of water in CNMs are generally classified into free, freezing-bound, and non-freezing-bound fractions as initially based on differential scanning calorimetry (DSC) melting and cooling curves and have been followed since then.[40] Furthermore, pore waters refer to water that occupies pores in the inter-fiber spaces and disordered regions and can comprise both free and bound waters. Whereas free waters have the same crystallization temperature as bulk water (peak I in **Figure 3a**), freezing-bound water has a relatively lower crystallization temperature (peak II in Figure 3a) indicative of water confinement in the cellulose structure. The difference between the sum of weights of water calculated from peaks I and II and the total water content is called non-freezing-bound water. The phase transition of non-freezing-bound water is not detectable as a first-order transition in DSC curves, and it is considered tightly bound to cellulose and the hardest to remove.

Although several indirect experimental correlations have been made to deduce water type, a direct method to distinguish freezing and non-freezing water has proven elusive. Recent work using ^{2}H NMR and ^{1}H NMR methods has identified mobile and immobile water sub-populations and proposed that the immobile and mobile water populations are present on the inter-fiber surfaces and inter-fibril surfaces, respectively, within a fiber (Figure 3b).[40,46,47] The water uptake of fibers has also been correlated with the degree of crystallinity in several works, often associating higher water contents with increased disordered regions in cellulose.[40,48–50]

3. Multiscale Computational Modeling of CNM in Solvents and CNM-polymer Nanocomposites for 3D Printing

Complementing experimental efforts to overcome CNM aggregation in solution and nanocomposites and to improve the

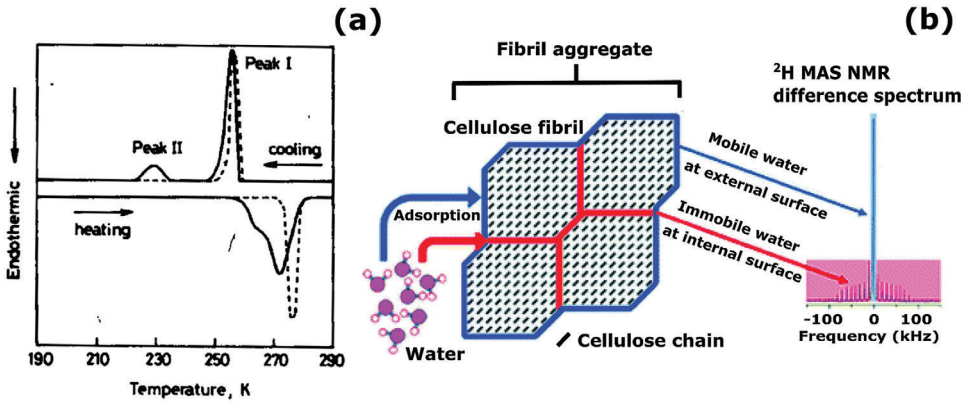

Figure 3. a) DSC curves of water adsorbed on various cellulose samples with heating and cooling rates of 8 K min^{-1}. Dashed lines (– – –) denote pure water, and solid lines (—) denote adsorbed water. Adapted with permission.[39] Copyright 1981, SAGE Publications Inc. b) Elucidation of mobile (blue) and immobile (red) water fractions around cellulose nanofibrils from the difference in the ^{2}H magic angle spinning (MAS) NMR spectra between the hydrated and re-dried samples. The high-intensity central peak (blue) denotes mobile water fraction before drying, and the broad peak (shaded in pink) denotes immobile water fraction after re-drying. Adapted with permission.[40] Copyright 1999, Royal Society of Chemistry.

stability of CNM-polymer interfaces, simulations at multiple length scales have provided insight into several factors that include the fundamental forces driving CNM aggregation and matrix-filler adhesion to predict long timescale dynamic properties, macroscopic flow parameters, and mechanical behavior of nanocomposites.[42,45,50–52] The insights obtained from these studies have contributed toward producing dispersed CNMs as AM feedstocks, improving AM processes, and mechanical evaluation of 3D printed nanocomposites.

Ab initio methods, including quantum-mechanical and DFT calculations, have provided an in-depth understanding of the structure and geometry, local charge environment of smaller glucan units/cellulose, and polymer chains in solution providing a backbone for the development of MD force fields.[53–57] DFT-based studies have also investigated the optoelectronic properties of conductive CNM-polymer nanocomposites.[58–60] However, in the context of CNM aggregation dynamics and polymer matrix compatibility for 3D printing in this review, we will not be discussing these methods in detail and will focus on findings from MD simulations and continuum modeling. Atomistic MD simulations have focused on understanding the effects of competing cellulose-cellulose versus cellulose-solvent interactions at various hierarchical levels and nanofibril and fiber conformational changes on CNM aggregation.[32,41,61–67] The free energy barriers of inter-fibril contacts between varying cellulose surfaces (hydrophobic vs hydrophilic), and native versus surface-modified fibrils have also been studied to predict chemically modified CNMs with reduced aggregation.[64,68,69] The interfacial structure distribution and mechanical strength of CNM-polymer nanocomposites have also been evaluated to improve CNM-polymer adhesion.[70–75] Coarse-grained (CG) simulations have been used to compute long time-scale dynamic properties on experimentally relevant timescales that include self-assembly of cellulose chains and bundles in solution, interfacial behavior, solvent evaporation, and phase ordering in specific classes of CNMs such as CNCs.[75–86] Continuum-level modeling includes mesoscale models, mainly FEM that has focused on evaluating macroscopic thermomechanical properties under different loading conditions and flow behavior in CNMs.[87–90] Below we outline a few important standalone simulation studies and combined experimental-simulation ones highlighting their main findings and later discuss how they can be utilized in the future for a synergistic experiment-multi-scale modeling to advance 3D printing of CNM-based materials.

3.1. Addressing CNM Aggregation Using Solvents and Surface Modifications

3.1.1. Thermodynamics of CNM Aggregation, Water Organization, and Self-assembly

One of the earliest CNM fiber studies on biomass pretreatment was performed by Langan et al.[50,62] at elevated temperatures (≈60–200 °C) where from small-angle neutron scattering and X-ray fiber diffraction experiments they observed nanofibril aggregation (**Figure 4a**) and an increase in crystalline domain sizes. MD simulations congruently showed fiber coalescence (aggregation) with an irreversible release into the bulk of inter-fibril (core) H_2O molecules at 160 °C. The core H_2O molecules formed stronger hydrogen bonds yet had a significantly lower rotational and translational entropy (ΔS) at 25 °C than bulk water indicating that inter-fibril hydration was enthalpically favored and entropically not favored. Upon increase in temperature to 160 °C, the core water hydrogen-bond interactions weaken due to an increased entropic penalty for confinement driving their release. Wohlert and co-workers[66] compared the dynamic relaxation behavior of cellulose chains in a fiber bundle in solution at 25 °C to experimental ^{13}C NMR spectra to quantify fibril regions based on their accessibility to water molecules. They discovered the role of hydroxymethyl conformational changes in varying relaxation behavior for the accessible and core regions. In a follow-up,[61] they calculated the Helmholtz free energy for transferring water molecules from the outer layer to inter-fibril spaces in a bundle ($\Delta F = \Delta E - T\Delta S$). ΔE was obtained from the difference in the MD potential energies between the native (hydrated fibrils) and fused states (aggregated fibrils) (Figure 4c) while the entropy term (ΔS) was estimated based on previously known

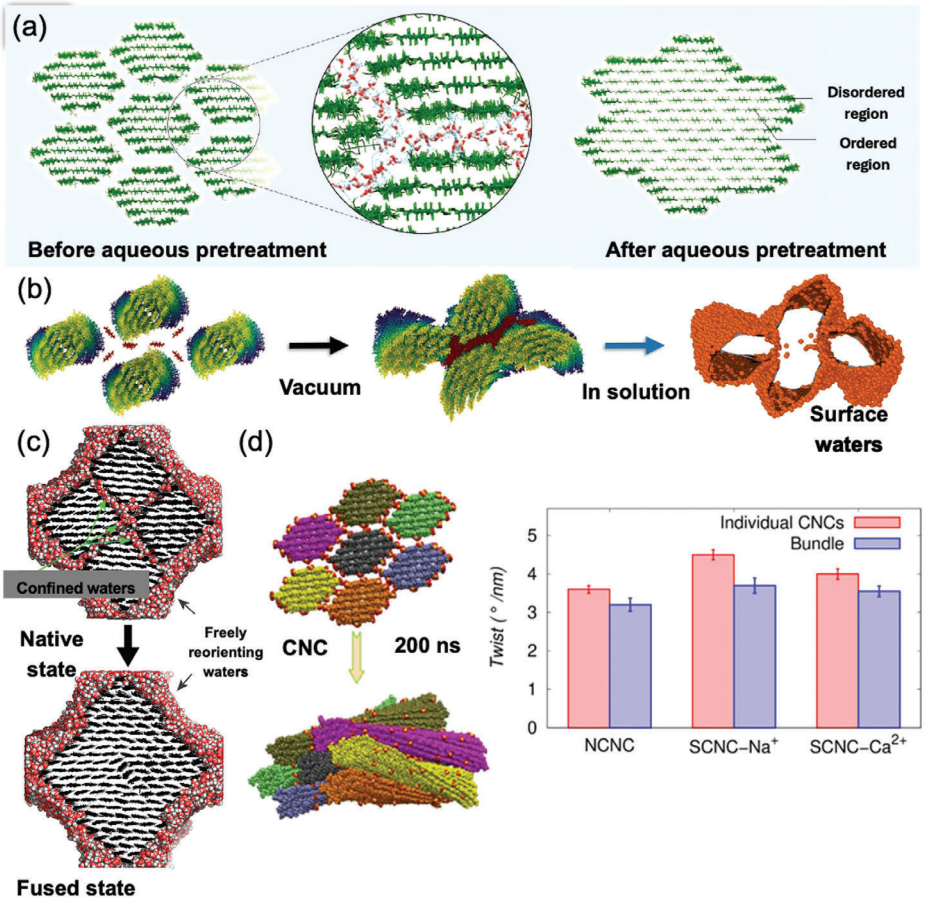

Figure 4. a) MD simulations from Langan et al.[50,62] showing the molecular organization of cellulose nanofibrils during steam explosion pretreatment (SEP). Before aqueous pretreatment, cellulose nanofibrils (green) are separated by layers of hydration H_2O (blue background), which is ordered relative to the bulk but disorders the cellulose surface (see inset with hydrogen bonds shown in blue, H in white, and O in red). At high temperatures, the entropic penalty of confining the hydration H_2O becomes too large, leading to its release. As a result, the cellulose fibrils coalesce to form a larger bundle. Adapted with permission.[62] Copyright 2018, Springer Nature. b) MD simulations with crystalline cellulose nanofibrils (green and violet) and six loose cellulose chains to mimic disordered regions (red) at 293 K first in vacuum followed by in solution. The surface water molecules (orange) are shown to be located mostly on the periphery of the fibrils, while a few diffuse into the bundle. Adapted under the terms of the CC-BY-4.0 license.[63] Copyright 2019, Springer Nature. c) The two states corresponding to hydrated and fused nanofibrils used by Chen et al.[61] to compute potential energies and entropy for water transfer from the outer shell to the inter-fibril core. Adapted under the terms of the CC-BY-4.0 license.[61] Copyright 2022, American Chemical Society. d) Twisting of a CNM bundle during 200 ns of all-atom MD simulations along with the plot that shows an increased twist rate for surface-modified CNMs with $OSO3^-$ groups and Na^+/Ca^{2+} counterions (SCNC/M^+) compared to native CNM (NCNC). Adapted with permission.[64] Copyright 2020, American Chemical Society.

values of molar entropy of fusion (ΔS_{fusion}) for water and differential change of entropy for water adsorption to cellulose ($\Delta\Delta S_{vapor}$). They obtained conservative estimates for ΔF ranging from ≈1 to 5 kcal mol^{-1} indicating that water transfer to the core was thermodynamically favorable at 25 °C. Paajanen and coworkers[63] compared the core and outer solvation shells for a cellulose bundle (Figure 4b) obtained from simulations at 25 °C to the freezing and non-freezing bound water contents measured from the melting DSC curves for bleached hardwood pulp. They also found the hydroxymethyl group conformational changes were important in introducing changes to the hierarchical structure producing a mismatch in the nanofibril versus bundle twist rates and concluded that this mismatch allowed water diffusion into the core. Zozoulenko and co-workers[64] similarly observed a positive correlation between fibril/bundle twist and inter-fibril aggregation in native and surface-modified fiber bundles where an increased degree of individual nanofibril and fiber twist resulted in an increase in inter-fibril gap (Figure 4d). The role of water molecules in nanofibril deformation and fibril-fibril interfacial strength has also been investigated using MD simulations.[65,67,91] Keten and coworkers[65] found that the tensile separation of fibril-fibril interfaces is less affected by the presence of water molecules compared to separation by shear. They further showed that the work of adhesion for shear separation was greater for the hydrophobic (200) than the hydrophilic (110) face. The interfacial behavior effects are attributed to water-water interactions competing with cellulose-water interactions which vary significantly depending on the hydrophobicity of the cellulose faces. Further work focusing on the 200 surfaces at varying interfacial water numbers and temperatures (298–350 K) showed that the shear work

showed a maximum moisture content (0.75% by weight) with varying water contents at different temperatures.[91] It was deduced that water at lower weight percentages acted as a "binder" providing a medium for improving inter-fibril interactions and consequently the interfacial strength. With a further increase in weight %, water functioned as a "lubricant" allowing an increase in inter-fibril gap and a decrease in interfacial strength. Drying MD simulations of wet inter-fibril interface showed a bending deformation of fibrils; the drying process elucidated the surface tension of the interfacial waters that created a concave meniscus during evaporation due to strong cellulose-water interactions accompanied by increased fibril-fibril adhesion.[67] Overall, these studies shed light on glucan chain conformations, inter-CNM and CNM-solvent hydrogen bonding dynamics, thermodynamic forces governing inter-fibril solvation and aggregation, drying mechanisms, and interfacial adhesion between fibrils at ambient and elevated temperatures.

Several cellulose CG models have been developed with a focus on understanding the crystalline mechanical properties and their conformational dynamics in solution. The most commonly used forcefield is MARTINI[76,77] which was parametrized and validated using experimental crystal lattice parameters, X-Ray and neutron-scattering data, elastic modulus, and water-octanol partitioning coefficients. MARTINI forcefields generally follow a mapping scheme of atoms: CG beads in the 4:1/3:1 ratio. MARTINI v3.0 force fields for cellulose improve upon the solubility, propensity for self-chain interactions, and native and surface-modified cellulose-ion interactions which were otherwise overestimated in MARTINI v2.0.[77–80] Other CG models have also focused on reproducing hydrogen bonding patterns in cellulose to predict assembly on longer time-scales for native and surface-modified cellulose fibrils, and the mechanical behavior of cellulose nanopaper which is on a much larger length scale.[81,82] Zozoulenko and coworkers developed supra-coarse-grained models that expand beyond the existing CG approaches in investigating the microsecond dynamics of crystalline CNCs.[83,84] These models with an implicit solvent approach can capture chiral nematic phase ordering, solvent evaporation, and formation of defects in CNCs.

Together, these studies provide a backbone to predict chemical modifications to surface hydroxyl groups, co-solvents with favorable physicochemical properties to interact with cellulose surfaces, and oligomers/molecules that physically interact with the cellulose surfaces to change their hydrophobicity. Their findings can be used to improve CNM properties for their better utilization as AM feedstocks.

3.1.2. Surface-Modified CNMs

Chemical modifications of the hydroxyl groups on glucan chains in CNMs have been explored computationally in solvents to overcome aggregation. The free energy cost for separation of 2,2,6,6-tetramethylpiperidine-1-oxyl radical (TEMPO)-oxidized nanofibrils simulated by Paajanen and coworkers[69,92] decreased significantly with increased percent conversion of hydroxymethyl (C6) OH groups to COO^- (**Figure 5**) which was associated with a decreased in inter-fibril hydrogen bonding for the modified systems compared to native cellulose fibrils (Figure 5b). Zozoulenko and co-workers[64] calculated potential mean force (PMFs) for the separation of OSO_3^- and COO^- modified fibrils with Na^+ and Ca^{2+} counterions for different faces in contact (hydrophobic vs hydrophilic). They further compared the inter-fibril gap for 7-nanofibril bundles of these chemically modified CNM systems (Figure 4d) in solution, with a native system. The separation free energy was reduced, and the inter-fibril gap increased for the OSO_3^- and COO^--modified systems compared to native CNMs with the reduction in aggregation being better for Na^+ compared to Ca^{2+} counter-ions. MARTINI-based CG MD simulations from the same group computed PMFs for TEMPO-oxidized and native CNMs reproducing atomistic simulations and adjusted the MARTINI parameters to reproduce native and charged cellulose interactions with ionic moieties NaCl.[79] They further provided a modular mapping framework for incorporating different surface modifications to cellulose surfaces that can be explored using less computationally intensive simulations.

Wohlert and coworkers[68] used thermodynamic integration and umbrella sampling methods to calculate the work of adhesion of separating acetylated versus native fibrils in solution from free energies between aggregated and dispersed states. They observed that the acetylated systems showed a reduced free energy barrier to remain dispersed compared to native fibrils in solution. Other simulations have also explored the effect of chemical modifications mainly COO^- and acetylated C6 hydroxyl groups on solvents and provided insights on electrostatic and van der Waals interactions that contribute to increased fibril-fibril repulsion.[45,93]

What is yet to be explored in detail is how design principles can be derived from modeling and experiments to identify specific chemical modifications that can improve compatibility with the commonly used thermoplastic polymer matrices for 3D printing such as PLA, PP, Nylon, acrylonitrile butadiene styrene (ABS) and PETG.

3.1.3. Co-solvent Driven Strategies

Exploiting the nature of different interacting cellulose faces in solution, alternate solvents and co-solvent systems have been investigated to manipulate cellulose structures in the context of both biomass pretreatment and biomaterials for 3D printing.[45,94–99] Sridhar et al.[45] performed wetting simulations for native and acetylated cellulose in solvents including water, hexane, ethanol, toluene, formamide, acetone, nitrobenzene, and dimethyl sulfoxide and found that the changing surface hydrophobicity did not reverse the affinities for water and other non-polar solvents. Smith and colleagues[95] showed that THF–H_2O mixtures exhibited significantly variable phase separation behavior at the hydrophobic and hydrophilic interfaces facilitating cellulose deconstruction (**Figure 6**). It was hypothesized that for an organic solvent to be effective in facilitating cellulose deconstruction, it must compete with cellulose for its hydrogen bonds as well as displace its hydrophobic stacking interactions.[94,95] MD simulations have also been performed to understand the interactions between cellulose fibrils/chains with other solvents, such as NaOH/urea/water mixtures and ionic liquids (ILs).[97,100–103] These simulations have shown that cellulose chains disperse at ambient temperatures in NaOH-urea-water and mostly at elevated temperatures (400–450 K) in ILs. Most of these simulations

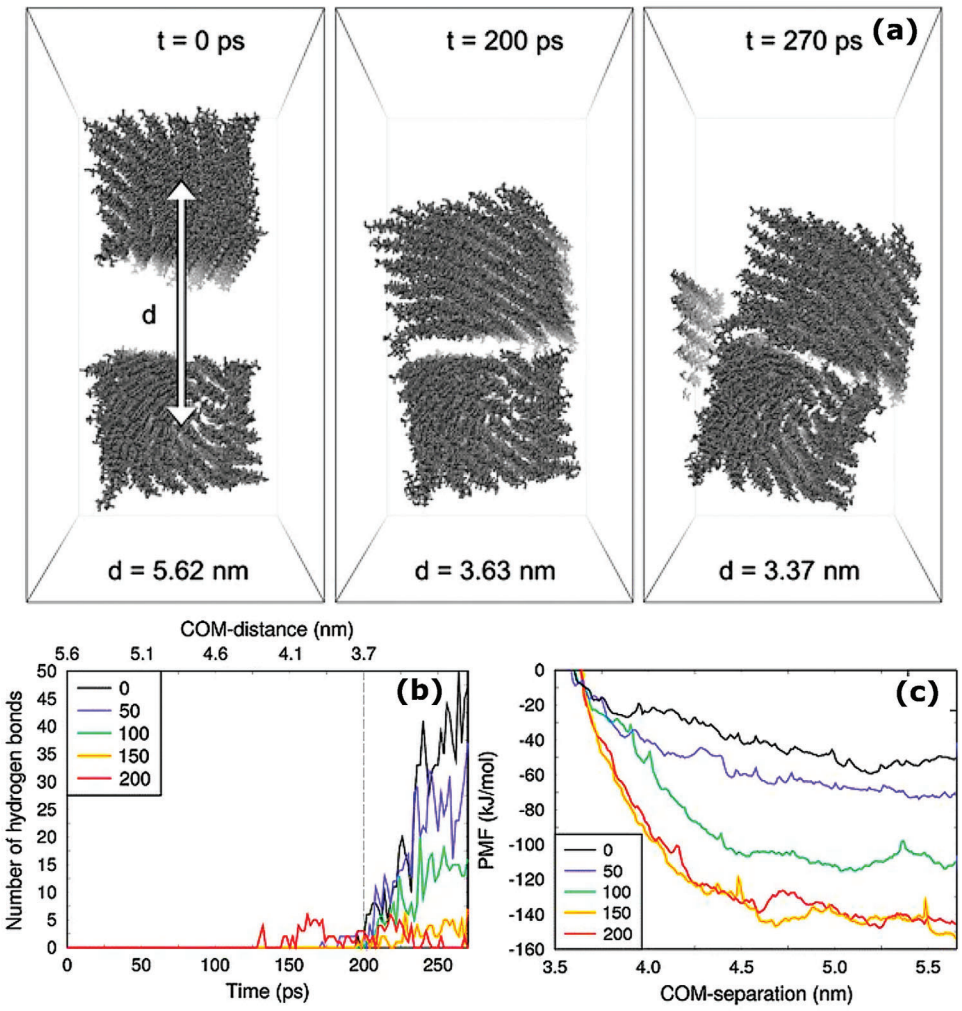

Figure 5. Umbrella sampling MD simulations of two TEMPO-oxidized nanofibrils: a) snapshots illustrating the pulling of fibrils toward each other at a constant rate of 0.01 nm ps^{-1}, displaying the distances, *d*, at different time intervals, b) increase in hydrogen bonds between the fibrils shown in (a) as a function of decreasing center-of-mass distances between fibrils, and c) free energy of separation of the fibrils shown in (a) with five curves denoting different functionalization levels of the fibrils (in terms of number of carboxylate groups substituted for C6 hydroxyl groups, 0 being the native CNF and 200 being 100% substitution). Adapted with permission.[69] Copyright 2022, American Chemical Society.

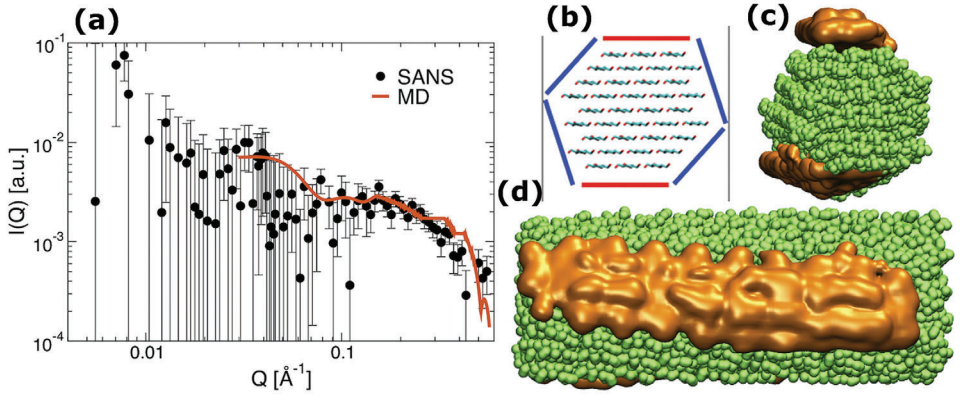

Figure 6. a) Excess SANS scattering of contrast-matched cellulose fibril in a THF-D_2O/ H_2O cosolvent minus the scattering of contrast-matched cellulose in D_2O, obtained from the experiment (symbols) and simulations (line). b) Surfaces of cellulose fiber are classified as non-polar (red) and polar (blue). c,d) Isosurfaces in which THF (orange) concentration is 3× higher than bulk, viewed perpendicular (c) and parallel (d) to the fiber axis. Cellulose is shown in green. Adapted under the terms of the CC-BY-NC-ND 4.0 license.[105] Copyright 2020, National Academy of Sciences – Biactive Work; National Academy of Sciences; Sdu; Birkhäuser Boston; Proceedings Of The National Academy Of Sciences.

to our knowledge have been performed on single nanofibrils or nanofibril-solvent interfaces that do not give us a direct understanding of their performance in inter-fibril or inter-CNM aggregation. Recent work by Liu et al.[104] computationally screened a set of 40 solvents that reduce inter-fibril contacts in a CNM bundle. They found that co-solvent mixtures containing hydrogen bond acceptor and donor moieties in conjunction with water such as gamma-Valerolactone (GVL)/NaOH-urea increased inter-fibril separation in a CNF (CNC) relative to neat water. Their pilot-scale experiments consistently showed a significantly reduced energy consumption during fibrillation for NaOH-urea-water by ≈21% compared to pure water. Although CG force fields have been developed to represent assembly in solution and solid-state properties, one that accurately predicts cellulose interactions with a diverse set of solvents (i.e., varying dominant interaction types such as van der Waals, hydrogen bonding, and electrostatic interactions) has not been explored to our knowledge. Existing CG models can be tested and improved by using both experimental and all-atom data on cellulose and solvent simulations. MARTINI v3.0 base models, for example, with parameters for various solvents including the traditional organic solvents, DES, and ILs can be tested and further optimized for predicting dispersion in a quick manner for systems closer to experimental length scales.

While the above simulation studies have given a few viable solvents for improving CNM dispersion, there exists a tremendous scope to develop a faster, large-scale computational approach to produce dispersed CNMs as AM feedstocks. MD-computed quantities for quantifying inter-fibril/inter-CNF contacts and energies from atomistic and CG simulations can be combined with thermodynamic (COSMO-RS)[106–108] models that can screen for solvents with better physicochemical properties such as low surface tension, low viscosity and better hydrogen bond participating capabilities. CNF contacts, energetics, and solvent properties can then be used to train machine-learning models to predict solvents that improve CNM dispersion.

3.2. CNF-Polymer Interfacial Structure, Adhesion, and Mechanical Behavior

MD simulation literature on CNM-based bionanocomposites is in general scarce, while the number of works focused on biopolymers used in 3D printing is even lower. Further, due to computer power limitations, most investigations have often used simple CNM units such as a nanofibrils.[70–74,92,109–114] The key goal remains to design CNM-polymer composites with optimal interfacial strength and mechanical properties and to thus improve manufacturing processes in an iterative and less cumbersome manner. As most thermoplastic polymers are hydrophobic, excluding a few with polar groups such as poly(3-hydroxybutyrate) (P3HB), polyoxymethylene (POM), and polyetherimide (PEI), it is difficult to design cellulose chemical surface modifications or physically interacting oligomers that can improve matrix-filler compatibility without compromising the elastic modulus.

Mottonen et al.[71] found an increase in modulus for cellulose–PP composites (**Figure 7a**) with an increase in the fraction of cellulose reinforcement (Young's modulus shown in Figure 7b) for a constant strain rate. The authors further investigated these composites in the presence of MAH as a coupling agent. MAH was first connected to a 50-mer PP chain, which was then covalently linked to the C6-OH group to form an ester, and a varying percentage of these chains was grafted to the cellulose fibrils. While the authors report that introducing MAH showed a minor increase in modulus (≈10% compared to native cellulose–PP), they acknowledge that their bonding methodology needs careful consideration. Glova et al.[70] designed PLA–CNC nanocomposites in which the CNCs were modified by grafting lactic acid oligomers on the C6 OH groups (Figure 7c) and found that the modulus did not vary significantly with change in percentage grafting, in contrast to experimental results (Figure 7d). The authors suggest that the difference could be due to the MD simulations being unable to capture long-timescale dynamics that could result in aggregation of cellulose. Ren et al.[70,73,115,116] studied nanocomposites containing amorphous cellulose and PLA and evaluated the tensile modulus, free volume, and distribution of intermolecular energies during deformation. Whereas the mechanical properties showed improvement upon incorporation of cellulose, the interface between PLA and cellulose weakened with increasing cellulose percentage, as cellulose–cellulose interactions increased to a greater extent than did the cellulose–PLA interactions (**Figure 8**).

Studies not limited to common thermoplastic CNM-composites used for 3D printing can still be used to develop robust multi-scale methodologies to understand and predict interfacial, physical, and mechanical properties. Zozoulenko and coworkers performed a combined experimental and all-atom simulation study of matrix-mediated stress transfer in poly(ethylene-stat-sodium acrylate)-CNC ($OSO3^-$/COO^- modified) nanocomposites. The authors showed that preferential cellulose-polymer interactions (over cellulose-cellulose interactions) through electrostatics and hydrogen bonding facilitated efficient stress transfer in the composite, maintaining the interface and mechanical strength. Keten and co-workers[75,117] developed both atomistic and CG models for CNC- and amorphous-cellulose-PMMA nanocomposites. They showed that the order of cellulose structures (CNC vs amorphous cellulose) impacts the packing of matrix polymer chains around cellulose and consequently cellulose-polymer interactions improving work of adhesion for amorphous systems. They further captured the positive effects of TEMPO-oxidation of CNCs on tuning glass-transition temperature under low and high reinforcement % and the associated interfacial strength. All-atom and CG simulations were performed on polyelectrolyte (PE)–CNF coacervates by Khan et al.[92] to improve mechanical properties and simultaneously provide an understanding of charged interactions between cationic–anionic PE and CNMs to modulate complex-CNM aggregation. MARTINI-based CG models have also been used to simulate conductive CNM-poly(3,4-ethylenedioxythiophene) (PEDOT):poly(styrene sulfonate) (PSS) nanocomposites to understand their morphology and interaction with cellulose interfaces.[85,86]

It is important to note that most MD simulations do not yet capture the inter-fibril/inter-CNF interactions and their effects on mechanical properties. Most of the simulation work so far has not focused on evolving design principles for thermoplastic polymers used in 3D printing such as ABS, nylon, PLA, PP, and PETG. For comparison and integration with 3D printing experiments of common thermoplastics, it will be important to

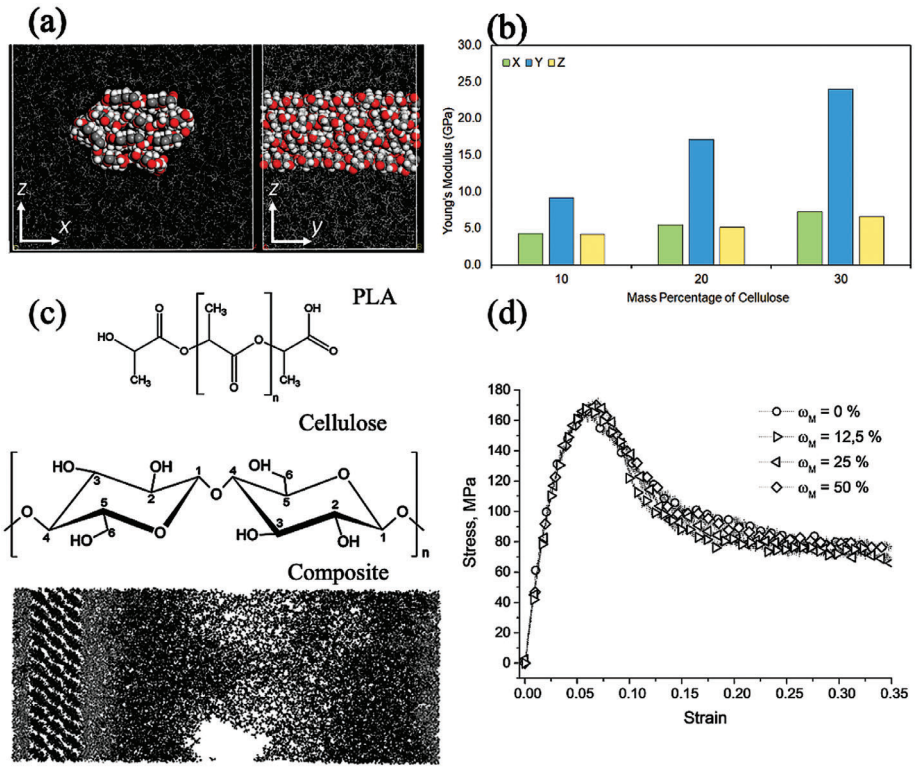

Figure 7. MD Simulations of crystalline cellulose–polymer nanocomposites: a) A cellulose–PP composite with 20% by weight of cellulose, presented in top and lateral view, showing the fibril arrangement and cellulose chains. b) Young's modulus of the composite (a) shown as a function of weight percent of cellulose for three orientations (X, Y, and Z shown in (a)) where the modulus shows an increase with increasing cellulose %, most prominent with respect to the X direction, perpendicular to the long axis of the cellulose chain. a,b) (Adapted under the terms of the CC-BY 4.0 license.[71] Copyright 2023, authors, MDPI, Basel, Switzerland c) PLA–cellulose nanocomposite showing the molecular structure of its components and a simulation snapshot of the interface (dark gray and light gray areas on the left show cellulose and the lactic acid oligomers grafted to its surface (50%), and the remaining black areas on the right represent PLA chains showing cavity (white) in between during stress–strain MD simulations. d) Stress–strain curves for the system in (c) at different grafting percentages (w_m) of lactic acid oligomers. c,d) Adapted with permission.[70] Copyright 1996, John Wiley & Sons Ltd.

simulate multiple crystalline nanofibrils and polymer matrices that are relevant for 3D printing. The forcefields further used in nanocomposite simulations for both polymers and CNF moieties must be chosen carefully to reproduce the experimental properties, such as tensile modulus, reasonably well. Another point to consider is that due to computational limitations, the strain rate in MD simulations is significantly higher than in the experiment—a well-recognized limitation in polymer MD simulation. However, the qualitative trends can still be meaningfully captured from MD simulations.[118,119] One of the major challenges would be to incorporate the effect of amorphous regions in a larger CNF in the context of AM-manufactured nanocomposites which is a non-trivial problem due to the heterogeneities that need to be sampled and a need for a rigorous approach drawing inspiration from some of the previous works mentioned above. Coarse-grained MD simulations and continuum models can be used to simulate large-scale systems similar to some of the CG methodologies presented above to evaluate CNF–polymer adhesion, material properties, mechanical strength, and viscoelastic behavior. The effects of molecular interactions in cellulose on properties such as viscosity, thermal conductivity, and modulus have not been studied extensively for CNM–polymer nanocomposites used in 3D printing. Although viscosity has not been computed for CNFs to our knowledge, combined experimental and simulation studies have been performed to compute the thermal conductivity of CNMs for an 18-chain nanofibril;[120,121] the thermal conductivity (κ) was found to be low, in the range of 0.5–2 W m^{-1} K^{-1}, making it promising for applications requiring low κ combined with high mechanical strength.[120,121] The low κ and amorphous-like behavior of κ was attributed to the strong boundary scattering of phonons due to the structure of CNFs comprising crystalline elementary nanofibrils and amorphous regions; however, κ was found to be independent of density and porosity, unlike typical amorphous or semicrystalline polymers. The effect of molecular interactions and the reason behind this anomalous behavior have not been investigated in detail and present scope for future study along with experimental validation and continuum models with the aim of obtaining optimal thermal properties and flow behavior for AM.

3.3. Finite Element Simulation of CNF Nanocomposites for Macroscopic Property Prediction

While molecular modeling methods offer an insight into dynamics, interactions, and associated mechanical strength, continuum

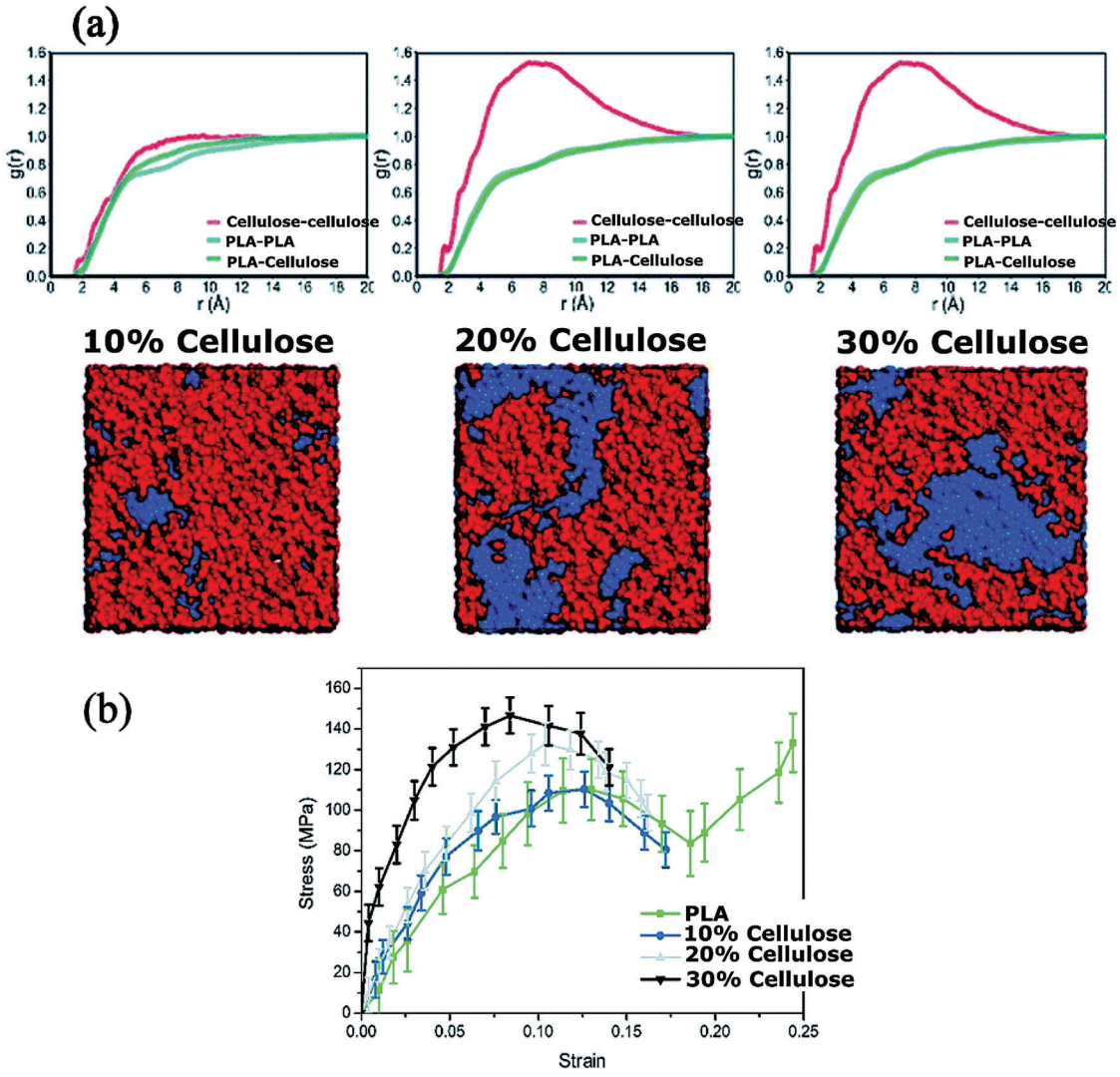

Figure 8. MD simulations of amorphous cellulose–PLA nanocomposites: a) Radial distribution function (g(r)) between cellulose–cellulose, cellulose–PLA, and PLA–PLA moieties with corresponding MD simulation snapshots showing distribution of cellulose and PLA in the nanocomposite for 10%, 20% and 30% by weight of cellulose reinforcement. PLA and cellulose form phase-separated clusters with increasing % of cellulose. b) Uniaxial tensile stress–strain curves for pure PLA, and PLA reinforced with 10%, 20%, and 30% by weight of cellulose, showing increasing strength with increasing cellulose percentage. Adapted with permission.[73] Copyright 2011, Royal Society of Chemistry.

models are highly reliable and accurate in capturing macroscopic mechanical behavior under different types of loading conditions including bending, shear, tensile, compressive, and oscillatory loads. They further capture long-time-scale diffusion and thermal behavior of nanocomposites that are on currently inaccessible timescales and are highly expensive. FEA is one of the most widely used methods to predict the mechanical properties of nanocomposites as summarized below.

Webo et al.[122] predicted flexural properties of mono and hybrid epoxy–resin nanocomposites, where CNFs extracted from sisal and/or rice husk nanoparticles were used as fillers. The authors found good agreement between the flexural strength predicted from FEA simulations and experimental data, observing an optimum point in fiber addition for flexural properties. Also, Mishnaevsky et al.[123] developed a 3D unit cell FEM with snake-shaped nano-cellulose fibrils, using ABAQUS/Standard to investigate material stiffness. Dhamodharan et al.[124] explored cellulose nanocrystal-decorated graphene oxide nanohybrids in a waterborne epoxy system, observing significant thermo-mechanical improvements at lower nanofiller concentrations, with numerical simulations again aligning well with laboratory values. Furthermore, Naddeo et al.[125] focused on cellulose acetate–graphene oxide nanocomposites, using a 3D FEM to study the influence of morphological parameters on Young's modulus, again achieving a good approximation of experimental trends. Li et al.[87] predicted the effective elastic properties of cellulose nanowhisker-reinforced composites through a microstructure-based FEA, and Zhang et al.[126] employed COMSOL Multiphysics 5.6 to study the tensile strength of a composite film with cellulose, polyvinylidene fluoride, and barium titanate nanoparticles,

confirming electrical breakdown behavior through simulation. Naddeo et al.[88] used a multiscale FEM to analyze the elastic behavior of graphene oxide nanocomposites, achieving a strong numerical–experimental correlation. Huang and Rodrigue[89] compared the mechanical properties of nanocomposites reinforced with single-wall carbon nanotubes and nanocrystalline cellulose under various loading conditions. Mohammadi et al.[90] applied a Galerkin-based non-linear finite element method to analyze the mechanical behavior of a polymeric aortic heart valve made of polyvinyl alcohol (PVA)–bacterial cellulose nanocomposite. Finally, Gao et al.[127] combined mechanical testing, microstructural analysis, and discontinuous FEM to study the stiffness of bacterial cellulose nanofibers, successfully calibrating their model with experimental data. The above studies collectively highlight the versatility and efficacy of FEA in advancing our understanding of the mechanical properties of various nanocomposites and composite materials.

FEA has also been effectively employed to study the viscoelastic properties of nanocomposites. Huang et al.[128] focused on the damage failure history of a conductive tough hydrogel, combining covalent cross–linking with metal coordination and silver nanowire reinforcement; they found that their finite element method-based stress–strain calculations aligned well with experimental data under tensile loading. Shojaeiarani et al.[129] investigated the nonlinear behavior of CNC-reinforced PLA composites, using a hyper-viscoelastic model with a neo-Hookean strain energy function and time-dependent Prony series. This approach, implemented in Abaqus/Standard, accurately determined material constants, mirroring both short and long-term experimental stress–strain data. Shakil et al.[130] explored the temperature-dependent mechanical and creep behavior of graphene oxide, silk fibroin, and cellulose nanocrystal nanocomposite, using a two-layer, viscoelasticity-theory-based FEM. They observed significant increases in hardness, reduced modulus, and yield strength, along with decreased creep displacements in the nanocomposite with a temperature rise from 25 to 80 °C. In summary, these studies highlight the precision and applicability of viscoelastic numerical models in FEA for understanding complex nanocomposite behaviors.

Zhao et al.[131] used the FEA package ANSYS to investigate heat transfer in the models of isotropic PP and multi-walled carbon nanotubes (MWCNTs) blends and multilayered anisotropic conductive polymer composites (ACPCs) in different directions. In addition, FEA was employed for a thermally conductive simulation to understand the effect of multilayered structures on the heat dissipation property of such ACPCs. In other work, Htira et al.[132] and Almahmoud[133] conducted significant studies on the diffusivity properties of nanocomposites using advanced computational methods; these studies focused on effective diffusivity in polynomial nanocomposite systems with rod-like nanofillers, employing COMSOL Multiphysics v5.4 for FEA. They modeled a representative volume element using an unstructured mesh of four-node tetrahedral elements, with automatic mesh refinement near the fillers to enhance accuracy, and studied the effects of variables like filler volume fraction, aspect ratio, and polydispersity. Almahmoud[133] undertook a multiscale design analysis and optimization, examining a membrane moisture exchanger for air dehumidification at the macroscale and water vapor diffusion in polymer nanocomposites at the nanoscale. This study utilized COMSOL Multiphysics for macroscale modeling and MAPS 4.3 and LAMMPS software packages for MD modeling at the nanoscale. Both studies highlight the integration of finite element methods and MD modeling toward understanding and optimizing the diffusivity properties of nanocomposites, contributing valuable insights for materials science and environmental engineering applications.

The FEA studies reviewed above highlight the usefulness of predicting complex mechanical behavior under different loading conditions and the viscoelastic properties for diverse nanocomposite systems, including CNMs in polymer matrices. Furthermore, the thermomechanical behavior and failure modes are also systematically evaluated in these studies, which provides valuable predictions of material performance under service conditions, thereby reducing experimental costs significantly. The FEA methodologies can be extended to novel CNM-based composite systems containing different CNM morphologies, surface modifications, and polymer matrices to produce a systematic correlation between changing molecular structure and material properties—including flow behavior, mechanical strength, and temperature-dependent mechanical performance. Literature shows us that there is a limited amount of research toward FEA of additive manufacturing processes for CNF-based nanocomposites. The common additive manufacturing technology for CNF-based nanocomposites are extrusion-based printing (e.g., FDM), which extrudes CNF-composite through a heated nozzle in a layer-by-layer process, where the material cools and solidifies after each layer. The material feeding rate, nozzle head moving speed, nozzle heating temperature, and ambient temperature influence the material properties of CNF composites. Direct ink writing is another AM technology for CNF-composites fabrication, which extrudes the past-like CNF mixtures through a nozzle with the need for heating, which is suited for CNFs as it requires lower viscosity and can incorporate higher CNF content. Stereolithography (SLA) is also a popular AM technique for CNFS when the CNFs are incorporated into a UV-curable resin, which provides a high resolution of the fabricated materials. Future work should consider the impact of AM process parameters on the CNFs distribution on the nanocomposites and the temperature effect-induced thermal residual stress, whose effect can be captured through nonlinear finite element method-based multiscale models where the thermal effect-induced change in the MD should be considered in the selected RVE in the microscale modeling based material properties calculations.

3.4. Integrating Multiscale-modeling and Experiment to Accelerate Additive Manufacturing with CNM-Nanocomposites

The above sections discuss some of the major challenges involved in utilizing CNMs as AM feedstocks and mixing them with polymer melts to achieve optimal adhesion, mechanical, and thermal properties for replacing traditional fillers in 3D printed applications, including aggregation and weak interface strength and compatibility. Prior experiments and simulations have focused on understanding the origins and addressing several facets of the problem both independently and collaboratively. However, with the advances in high-performance computing and modeling methods, an integrated approach exploiting various

computational techniques can accelerate the discovery and advancement of materials and processes relevant to 3D printing of the CNM nanocomposites on a large-scale. Further, recent advances in machine learning methods can be utilized with conventional modeling techniques to fill in the current gaps in consistent data to quantify and predict dispersion and adhesion. The aim of using computation is to be able to screen many times more possibilities than can experiment, while also providing an understanding of design principles needed.

While QM/DFT simulations have provided robust forcefields for MD simulations of cellulose-solvents and cellulose-polymer matrices, MARTINI-based CG simulations can be used to compute properties including material density (ρ), viscosity (η), modulus (σ_e) for different CNM surface modifications and thermoplastic polymers relevant for 3D printing applications. The systems can then be screened for high-performing materials whose composition and properties can then be given as input to the FEM simulations. FEM simulations will then evaluate macroscopic properties: thermal conductivity (κ), diffusivity (D), mechanical strength under different loading conditions (shear, tensile, compressive, flexural, creep), flow rate, and failure modes (void and crack propagation). The materials can then be given an overall score based on the above metrics of material and mechanical properties where the ones with the highest score will then be prioritized for experiments. Experimental parameters such as energy requirement for fibrillation, CNM dispersion/interfacial behavior through microscopy (scanning electron microscopy, atomic force microscopy), suspension, and composite rheological measurements (for example viscosity) in turn can inform modeling to optimize both MD and FEM optimization. A schematic showing this multi-scaling modeling-experimental pipeline is presented in **Figure 9a**.

In the future, a minimalistic MD model using all-atom and CG simulations may be able to be used to compute fibril interfacial/contact energies, screening through many solvents and polymers to find those with promising performance. Machine learning models might then be employed to derive trends between solvent and polymer physicochemical/mechanical/viscoelastic/thermal properties in the literature[134] and the MD-computed energies to identify the important features governing CNM aggregation and dispersion such as hydrogen bond propensities and surface tension. Properties (ρ, η, σ_e) can then be obtained for composites with features that contribute positively to reducing aggregation and improving dispersion in matrices and fed into FEM to accelerate the process. A multi-scale modeling strategy for fiber-reinforced polymer composite models was provided by Lin and Zhang[135] (Figure 9b) where modeling techniques can be used to address various experimental challenges: interface phenomena using all-atom free energy calculations, capillary action of fluids with these composites using continuum modeling, relaxation time and aging of polymer chains from CG simulations, and degradation mechanisms using kinetic MC methods. The complex nature of interactions and organization in cellulose-based nanocomposites put together with the required rheological and material properties to facilitate 3D printing necessitate the use of multi-scale approaches to tune the morphology and properties mentioned above; further future studies employing some of the FRP methods can be used to augment this pipeline.

4. High-Performance Applications of CNMs in Additive Manufacturing

While computational modeling can design and predict the CNM drying, and CNM-polymer composite properties, it is imperative to provide examples of applications where these simulations can help design materials with better properties. So far, we have discussed pure CNM and CNM composite properties obtained from fundamental understanding-based computer simulations at different lengths and time scales. In this section, we will identify three specific applications where a synergistic approach between simulations and experiments can be used to produce materials at a large-scale in a cost-effective way from the basic understanding of simulations at the nanoscale. We start this section with a discussion on 3D printing techniques, followed by applications in feedstocks in structural nanocomposites, food packaging, flexible electronics, and microfluidic devices, and end with hydrogel-based scaffolds for biomedical applications. The techniques used for 3D printing in the preparation of cellulose nanomaterials (CNMs) primarily include two categories: extrusion-based and vat polymerization.[138,139] In extrusion-based approaches, shear-thinning fluids are extruded from a nozzle onto a platform in a layer-by-layer manner, thereby forming a three-dimensional object. This category includes fused deposition modeling (FDM, also referred to as fused filament fabrication or FFF) and direct ink writing (DIW). For FDM, as illustrated in **Figure 10a**, the prefabricated filament is continuously fed into the heated liquefier (with the temperature determined by the polymeric material) through mechanical systems.[140,141] The molten end is then extruded through a nozzle of a fixed diameter onto a plate, typically preheated to a specific temperature suited to the polymer matrix, forming the desired shape. In FDM-based 3D printing of CNMs composites, cellulose-based fillers are blended with a polymer matrix. The polymer matrix generally facilitates flowability during extrusion while maintaining the shape post-extrusion due to the shear-thinning behavior of the polymer network. It also provides essential mechanical strength. Meanwhile, the CNMs contribute to modifying the rheological properties during printing and functionalizing the printed materials due to their intrinsic characteristics, such as a high aspect ratio and the presence of abundant functional groups, which will be discussed in the following sections.

A significant challenge in FDM printing of CNMs composites is achieving homogeneous blending with the polymer matrix. The cellulose-based fillers need to be thoroughly dried; however, upon drying, the strong hydrogen bonding between CNMs can cause aggregation. This aggregation leads to difficulties in obtaining uniform dispersion within the polymer matrix, which negatively affects the interfacial adhesion between the two phases, as well as the overall mechanical performance of the composite.

Another extrusion-based 3D printing technique that can mitigate some of the challenges in FDM is direct ink writing (DIW). In DIW, as shown in Figure 10b, a formulated ink is extruded from a nozzle onto a platform via a pressure system to create an object layer by layer. Unlike FDM, which uses polymer melts for printing, DIW employs shear-thinning inks with varied components. The required property for the ink includes low resistance during extrusion, sufficient yield stress, and rapid elastic recovery after extrusion.[141] Thus, the formulation of the ink

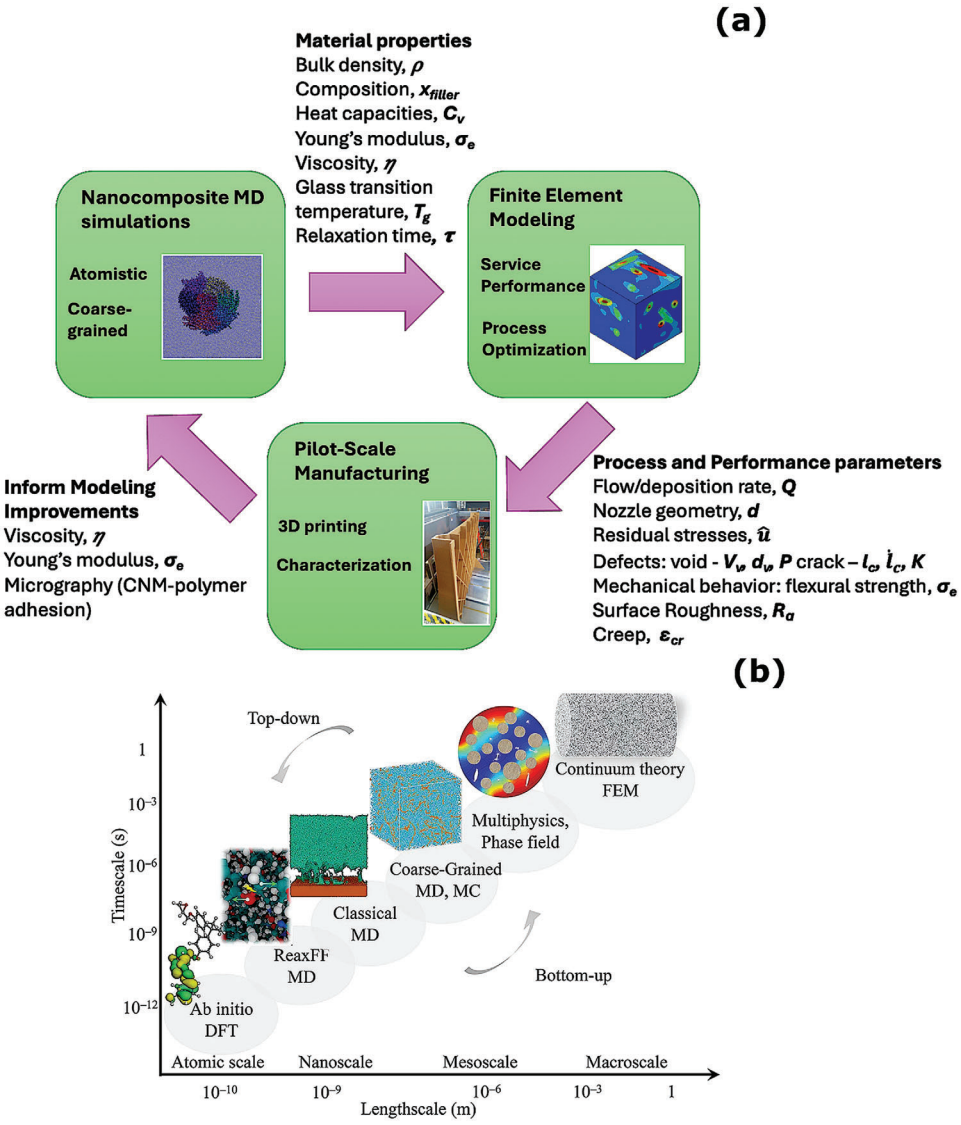

Figure 9. a) Schematic in the current review proposing future methods for integrating MD simulations (CG and atomistic), continuum FEM, and experiments to accelerate the materials design and process optimization of 3D printed nanocomposites. MD figure - unpublished, Experimental figure - unpublished, FEM figure – Adapted under the terms of the CC-BY 4.0 license.[137] Copyright 2020, Walter de Gruyter GmbH; De Gruyter; Freund. b) Multiscale Simulation framework that has been applied for fiber-polymer composites. Adapted under the terms of the CC-BY 4.0 license.[135] Copyright 2023, Nature Publishing Group UK; Nature Research; IEC.

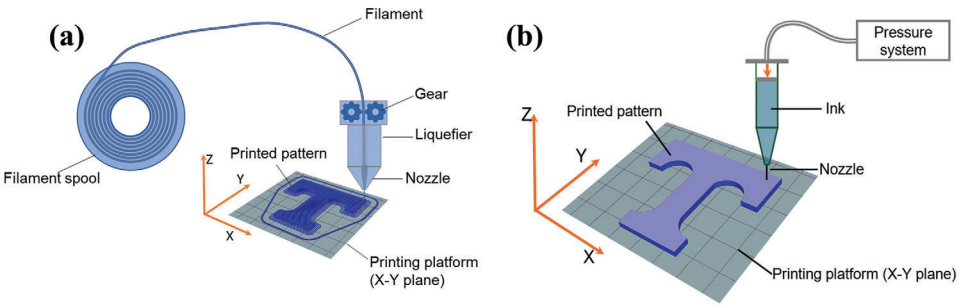

Figure 10. Extrusion-based 3D printing techniques. a) Fused Deposition Modeling (FDM), b) Direct Ink Writing (DIW). Adapted under the terms of the CC-BY-NC 4.0 license.[139] Copyright 2020, Royal Society of Chemistry.

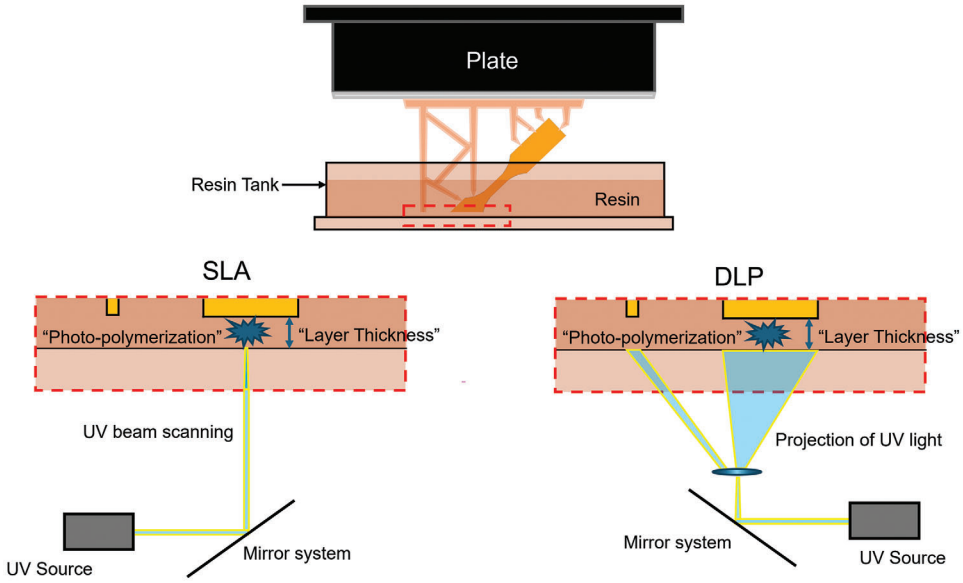

Figure 11. Vat photopolymerization 3D printing techniques. Adapted under the terms of the CC-BY-NC 4.0 license.[139] Copyright 2020, Royal Society of Chemistry.

needs to be carefully optimized to meet these printing requirements. For CNMs incorporated inks, they can be formulated from aqueous cellulose suspensions without drying, thereby avoiding aggregation. Adequate mixing is crucial when preparing CNM-based suspensions for DIW, especially for materials with anisotropic properties. Techniques such as homogenization,[142] speed mixing,[141,143] and sonication,[144,145] can be employed to achieve a homogeneous suspension. Additionally, a degassing process is typically applied prior to printing to ensure smooth extrusion.[141,146]

Two variants of DIW have been developed for printing cellulose-based composite materials. One is known as direct cryo writing (DCW).[147] In contrast to conventional DIW, DCW utilizes a cryogenic plate during printing, which allows the extruded material to freeze immediately, reducing the dependence on the rheological properties of the inks. Another variation, termed "matrix-assisted" DIW,[148] involves printing inside a matrix that helps maintain the printed architectures. This technique reduces the need for strict control over the rheological behavior of the ink. Both variants potentially broaden the range of reagents that can be used in ink formulations and expand the application possibilities for CNM-based materials.

In addition to extrusion-based 3D printing techniques, vat photopolymerization methods, such as stereolithography (SLA) and digital light projection (DLP), have also been employed for 3D printing with cellulose nanomaterials (CNMs).[139] Like extrusion-based techniques, vat photopolymerization builds objects layer by layer; however, the formation of each layer occurs through the polymerization of a photoreactive resin, initiated by UV light. In SLA, as illustrated in **Figure 11**, a printing plate is immersed in a tank containing photoreactive resin. During printing, the distance between the plate (or current working area) and the tank bottom is adjusted to control layer thickness. UV light scans each layer's pattern, initiating photopolymerization[149] Once a layer is completed, the plate is repositioned to accommodate the next layer. DLP follows a similar process, though each layer is printed by projecting the UV light pattern onto the resin.

When incorporating CNMs into vat photopolymerization, the dispersion of fillers presents significant challenges. The dried particles must be uniformly dispersed in the resin to prevent aggregation. Another issue arises from gravity-induced settling of the fillers during the printing process.[150] Furthermore, the loading concentration of fillers in the resin impacts the print quality, as excessive filler content can hinder UV light penetration, leading to additional complications.[151]

Compared to traditional manufacturing methods for CNMs, such as melt processing with polymers (including extrusion, injection molding, and resin transfer molding) and casting from CNM suspensions,[152,153] 3D printing can construct hierarchical architectures on different scales according to design specifications. This approach allows for the maximization of the structural features of CNMs, enabling their application in advanced, high-value contexts, following the structure-processing-property relationship. However, a significant limitation of CNMs 3D printing is a relatively slower production rate compared to traditional ones, highlighting the need for further research to address this challenge and improve the efficiency of the process.

5. CNMs as Additive Manufacturing Feedstocks for Structural Nanocomposites

Structural or load-bearing applications for materials are abundant, both small (such as mounting brackets or pillars in a car or furniture) and large (such as bridges, buildings, etc.). Indeed, cellulose-based materials are some of the oldest structural materials. Important material properties for structural applications are the material's elastic modulus (i.e., stiffness), strength, and toughness. As discussed above, cellulose is a desirable structural material due to its relative abundance and high specific mechanical properties; CNMs have therefore been

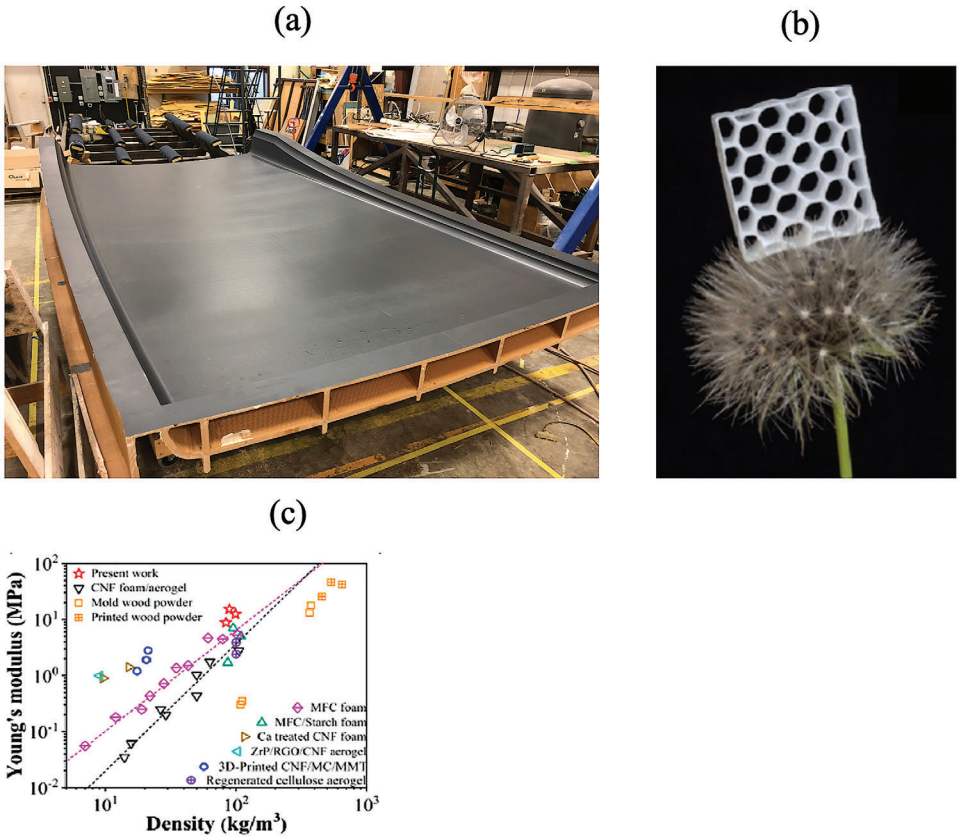

Figure 12. Additive manufacturing of structural materials on a large scale and a small scale. a) Large-scale AM of a yacht printed from 20% Wood Flour + 1% Cellulose Nanofibril + PLA (unpublished) b) Small-scale material extrusion prints of an all-CNF hexagonal lattice structure showing c) exceptional specific stiffness. (b-c) Adapted with permission.[161] Copyright 2021, Elsevier B.V.

investigated for the development of structural bulk materials, including with CNF-rich composites[154–157] and in various thermoplastic and thermoset composites to improve properties, and these have been documented in various review papers.[113,158, 159] While processing methods and bulk material properties for CNM composites are numerous, CNMs have not been extensively explored in 3D printed structural applications, which may be due partly to the outstanding need for validation of 3D printed parts for structural application and partly because of the availability of these materials or lack of development for AM feedstock. The subsequent paragraphs focus on the application of these materials in 3D printed structural applications, drawing from cellulose-based feedstock 3D printing applications where necessary to highlight development opportunities.

Cellulose-based fillers have been used in large-scale 3D-printed structures such as the bamboo-filled PLA high-top bar and arching pavilion for the Miami Design Expedition in 2016,[160] wood-CNF filled PLA for boat roof mold in 2018,[136] a lightweight, super-strong yet flexible all-cellulose structure,[161] and in the wood-filled PLA BioHome3D at the University of Maine in 2023,[162] all large structural applications. In these applications, up to 20 wt.% of filler was used to improve printability (i.e., rheology, shape retention/form stability) and provide a competitive alternative to carbon fiber–reinforced ABS for large-scale AM, at least in terms of printability and forecast cost, while remaining renewably sourced.[136,160,162,163]

A common interest between general composite applications and AM structural applications in incorporating CNMs into composites is to improve the mechanical performance of the composite as these high aspect ratio nanoparticles are strong, stiff, and low-density.[113] Gardener et al.[136] examined the use of CNF as both the primary filler and as a hybrid filler system (two unique fillers/reinforcements) in PP, styrene maleic anhydride, and PLA for feedstock to manufacture a boat roof mold. The PLA material systems showed the most significant improvement in compressive stiffness and strength by adding 10% CNF; a PLA formulation containing 20 wt% wood flour and 1% CNF was ultimately selected.[136] **Figure 12a** shows another large-scale 3D printed yacht from the same group made from 20% wood flour, 1% cellulose nanofibril, and PLA with superior mechanical properties (unpublished).[136] Other studies have shown an improvement in PLA properties with the addition of CNF for 3D printing applications, as well as the embrittlement that has also been observed in bulk composite property studies, especially at significant loadings.[163,164] As previously mentioned, one of the challenges with CNM composites, particularly those aiming to target large-scale AM, is the dispersion of the CNMs in the polymer feedstock. It is well documented that CNMs agglomerate during drying, and strong inter-CNF hydrogen bonding resists

re-dispersion in the polymer matrix, resulting in the distribution of micron and sub-micron particles.[165] For those looking to scale CNM composites for structural applications, this means producing large quantities of composite pellets to be used on medium- or large-scale pellet-fed material extrusion systems (e.g., 3DP workstation, Big Area Additive Manufacturing, Juggerbot).

CNFs are often added to polymers to improve the mechanical properties, specifically the stiffness and strength of the composite; however, this can also lead to improvements in competing effects like enhanced crystallinity and reduced coefficient of thermal expansion (CTE)—properties that are of practical importance for AM. In AM, warpage/distortion and delamination during printing are often caused by the buildup of residual stress in the material, as it contracts during cooling: the layer being printed is being deposited on a previous layer, which has already cooled and contracted to an extent. Moreover, crystallization can cause a high level of shrinkage (densification); consequently, the materials seen as having the highest printability are often slow-crystallizing polymers like PLA or amorphous polymers like ABS. However, the addition of CNMs to semi-crystalline polymers demonstrated that these materials can be heterogeneous nucleation agents, improving both the rate of crystallization in the polymer as well as the degree of crystallinity.[166–169] Despite those improvements, the effects are dependent on several variables, such as material system, dispersion level, solids loading, as well as processing variables like bed temperature or cooling rate (in AM, this would be related to layer time, distance from the print head, etc.). In the case of CNF-PLA composites, at mild bed temperatures, the addition of CNF has been observed to increase the total crystallinity relative to neat PLA, resulting in enhanced strength and stiffness.[170] In large-scale AM, there is an opportunity to better understand how CNMs might affect the CTE of polymer feedstocks and crystallization rates for semi-crystalline polymer feedstocks. AM of CNF-containing thermoplastics has shown this to be true for shear-induced orientation.[25,161,171–173] Printing of CNF composites results in a distribution of oriented CNF and CNF bundles along the print direction, like other rigid particles such as carbon fiber or alumina platelets. However, unlike rigid particles, due to the flexibility and irregular shape of these materials, CNFs have been observed also to exhibit different degrees of extension, which can affect the mechanical properties.[171] CNMS are well-known rheology modifiers, even at small concentrations, and in the development of AM feedstocks, these materials have been shown to significantly increase the viscosity of the polymer melt and change the rheological behavior.[165]

It is worth comparing the AM of composites containing CNFs versus CNCs at this point to understand the effect of crystallinity, particle sizes, morphologies, and processing/pretreatment techniques on the properties that are relevant for structural applications. The fundamental structural difference between CNCs and CNFs is the absence of amorphous fragments in the former as opposed to the latter; CNFs contain both crystalline and amorphous domains resulting in differing dimensions and high aspect ratios. The degrees of crystallinity for the longer CNFs (70%) are lower than those of CNCs (> 85%), and they form entanglements at lower concentrations compared to CNCs (1 wt.% for CNFs as compared to 10 wt.% for CNCs).[174] CNFs are known to exhibit higher solution viscosities than CNCs owing to several factors, including the presence of entanglements at a relatively lower concentration, wide size distribution of fibers, and inter-particle interactions. These factors also affect the optical properties, fiber alignment, and thus the mechanical strength of CNF- versus CNC–polymer-based composites. Fiber alignment during AM to improve mechanical strength and toughness was performed by Li et al.[159]: results showed greater order parameters, which translates to higher strength and stiffness, for long CNFs (590 nm, 683 nm) compared to shorter CNFs (390 nm).

Structural and mechanical properties were studied with PEO-CNC/CNF composites by Xu et al., and the results showed that the CNFs and CNCs produced had similar diameters but differed significantly in their lengths (i.e., 150 nm vs 1 μm). The addition of CNFs resulted in a relatively higher Young's modulus (by 100 MPa at lower reinforcement % and up to 500 MPa at higher values up to 10%) and a lower strain-at-failure compared to CNCs.[35] Another recent work involving a comparison of CNF- versus CNC-based composites was performed with vegetable oil polymer resin,[175] where it was shown that the thermal properties of CNF-based composites were superior to CNCs, whereas the stiffness was higher in CNC-based composites above the glass transition temperature of the resin, as shown by the storage and loss moduli values. It is important to note here that a direct comparison of CNF versus CNC-based polymer composites across different studies is non-trivial and must be done cautiously because the morphology, particle sizes, aspect ratios, pretreatment/hydrolysis method, and, consequently, the degree of crystallinity can show significant variations between studies.

CNMs have demonstrated remarkable strength and stiffness-to-weight performance in all-cellulose and cellulose-rich composites, and additively manufactured materials are no exception. While no structural applications for these materials have yet been realized, the high specific stiffness of these materials warrants a brief review. The AM of hydrogels, cellulose paste, and cellulose foams using material extrusion processes leverages strong hydrogen bonds on the cellulose structure to create AM materials with potential use in structural applications (Figure 12b,c).[161] The high viscosity and shear-thinning qualities of the CNMs, which, as discussed previously, can be utilized as rheology modifiers in composite systems to improve printability, are conducive to printing inks or suspensions for the material extrusion processes like direct ink writing (DIW).[25,93,104–106,161,172,173] However, a potential limitation of working with the water-based suspension is increasing the CNM content. Currently, most inks that have been developed have low concentrations (<10%),[25,161] although there are some examples of higher concentrations.[172,173] With a significant water content in CNM inks, the printed part will undergo significant shrinkage, potential cracking, and distortion during drying because the majority of the component is water.[173] For instance, a study by Jiang et al.[161] showed high volumetric shrinkage rates, >60%, for suspensions containing 4–6% CNF as well as anisotropic shrinkage (Figure 12b,c). This issue can be mitigated somewhat by controlling the drying conditions; for example, Klar et al.[173] observed that at faster drying rates or higher drying temperatures, the shrinkage was reduced. These materials could find application in areas that require high specific strength or stiffness, such as those in buildings and construction or in niche packaging applications, in addition to biomedical.

6. CNMs for Food Packaging, Flexible Electronics, and Microfluidic Devices

We now summarize various trial applications of CNF and CNCs in small-scale 3D printing. In the study lead by Zhou et al., a core–shell square scaffold was prepared by coaxial AM to increase the shelf-life of litchi fruits and develop intelligent packaging.[176] The core contained 1-methylcyclopropene (1-MCP) and chitosan, and the shell contained anthocyanin (a pH-responsive dye) that prevented the interaction of these two additives with each other. 1-MCP is a non-toxic film additive that can delay ripening because it is an ethylene receptor inhibitor. However, it has to be distributed in a polymer matrix to reduce its volatility for slow release. The food dye changes its color from blue-purple to red-pink on the decrease in pH due to an increase in the acidity of fruit upon spoilage. The core solution contained chitosan, lactic acid, and 1-MCP. The shell solution contained CNF, sodium alginate, κ-carrageenan, and anthocyanin. The solutions were extruded through syringes, and the fresh scaffold was immediately sprayed with 2% $CaCl_2$/2% KCl to cross-link the alginate that locked the shape of the extruded roads and layers; this alginate was then freeze-dried to form the scaffold. The presence of CNFs gave the solution appropriate shear-thinning behavior for extrusion and prevented the scaffold from collapsing upon freeze-drying. The presence of the scaffold in the litchi container increased the shelf-life by 6 days, which was easily detected by the blue color of the scaffold and the lack of fungal mycelia on the surfaces of the fruits (**Figure 13**).[176]

In another printing application, starch or milk powder was mixed with CNF, followed by a mixing of plant protein concentrate and rice bran to form a food paste that was printed by DIW. The addition of 1.5% CNF provided the appropriate viscosity and shape retention, and it reduced the hardness compared to prints without CNF.[177] Printing of CNF requires appropriate paste-like viscosity for the printed extrudate to hold the desired shape. The addition of locust bean gum to a 1% CNF aqueous suspension—in a ratio of 3–5 parts locust bean gum to 1 part CNF—improved the viscoelastic behavior. This enhancement led to better printability and greater dimensional stability of the dried printed scaffolds.[178] CNC has a different viscoelastic behavior than CNF. Increasing the concentration of CNC to form pastes can increase printer nozzle clogging. Therefore, electrostatically stabilized nanocrystalline cellulose (ENCC) was applied as an additive to increase the viscosity of dilute CNC suspension to improve printability and improve mechanical strength. ENCC was prepared by periodate and chlorite oxidation to break the C2–C3 bond of glucose and form carboxylic groups. Experimenters added 50 mM $NaHCO_3$ to a 10% mixture of 1:2 to 2:1 ratio of CNC/ENCC for network formation and screening the highly anionic ENCC from electrostatic repulsion among the chains that increased the compressive strength by 78% compared to CNC cryogels.[179]

CNF, methylcellulose (MC), montmorillonite (MMT), glyoxal (0.58%), and tannic acid (0.02%) were combined to produce foams and were printed by DIW for use as a packaging, thermal insulation, or adsorption material. MMT had the role of a rheology modifier, MC as a surfactant-like additive, glyoxal as a cross-linking agent, and tannic acid as a foam stabilizer in TEMPO-oxidized CNF paste. Glyoxal is commonly used as a paper-strengthening agent and improves the wet strength of cellulose. Foaming was done by using a whisk and stirrer. Drying of fresh prints at 80 °C caused annealing of MC that stabilized the printed shapes and showed <10% shrinkage. The optimized foam had a bulk density of 21 kg m^{-3}, 2.8 GPa tensile modulus, and 113 kPa tensile strength.[180]

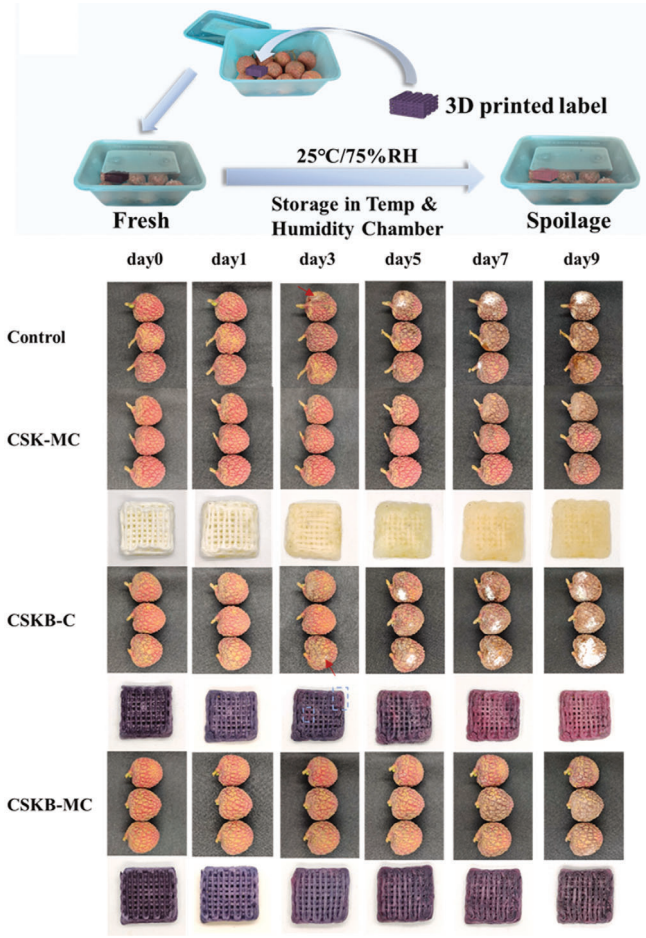

Figure 13. Schematic diagram of the freshness monitoring and preservation experiment of litchis. The figure shows a color-changing printed scaffold made from CNF/sodium alginate/k-carrageenan/blueberry anthocyanin/chitosan, without and with 1-MCP (reduces fruit ripening). Adapted with permission.[176] Copyright 2021, Elsevier Ltd.

To form conductive composites for energy management and wearable electronics of various shapes, carbon nanotubes (CNTs)/CNF at a 1:1 ratio have been 3D printed. For this CNF was oxidized using TEMPO radical and mixed with CNT to form a viscous gel.[165] The gel was printed using a syringe, followed by water removal using ethanol. Oxidized CNF acted by electrostatic repulsion and possibly hydrophobic interaction with CNT to prevent aggregation of CNT. The print had high electrical conductivity (216.7 S cm^{-1}) due to good distribution of CNT and high tensile strength (247 MPa) due to the presence of CNF and CNT.[181] In another study, carboxymethylated CNF was printed and then immersed in a CaCl2 bath for cross-linking for the print to hold shape once dried. Drying was carried out by solvent exchange using hexane, ethanol, and acetone to reduce pore collapse. To make

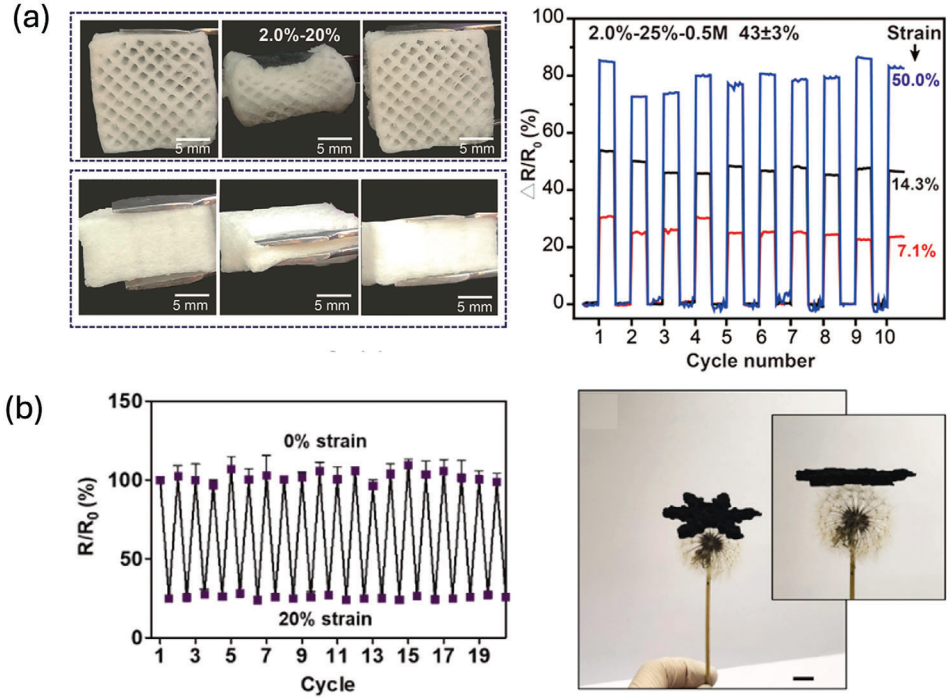

Figure 14. a) Shape recovery photos of 3D-printed 2.0% CNF, 20% infill monolith after both in-plane (top) and out-of-plane (bottom) compression. The relative resistance changes of 2.0% CNF, 25% infill density, and 0.5 M $CaCl_2$ monolith under cyclic compression at 7.1%, 14.3%, and 50.0% strains for 10 compressive cycles. Adapted with permission.[185] Copyright 2021, American Chemical Society b) Cycling tests of the polypyrrole-CNF foam. The compression cycle was repeated 20 times at 0% and 20% strains. Super-light lightweight conductive polypyrrole-CNF foam placed on dandelion seeds. Adapted with permission.[186] Copyright 2020, Elsevier Ltd.

the ink conductive, CNT and cetrimonium bromide (CTAB) surfactant (for dispersion) were added to the CNF, but the conductivity was only 0.01 S cm^{-1}.[182]

CNCs were added to methacrylate malate photocurable resin (MMPR) to obtain high dielectric constant composites for flexible electronics. The photocurable resin was synthesized by adding initiators and reacting neopentyl glycol, diethylene glycol, phthalic anhydride, malic acid, and methacrylic acid. CNC, methacrylic acid, potassium persulfate (catalyst), and 4-hydroxy-2,2,6,6-tetramethyl-piperidinooxy (ZJ-701) (cross-linking initiator) were reacted at 70 °C for 6 h; the unreacted chemicals were removed, and the suspension was freeze-dried to obtain CNC-methacrylate powder. This powder was added to the resin along with 2,4,6-trimethylbenzoyl diphenylphosphine oxide (TPO) (photoinitiator) to prepare photocurable composite resins. Ring capacitors with 0–1% CNC were prepared by stereolithography AM using UV light. Due to the addition of CNC, tensile strength of 16–18 MPa and 33–39% elongation could be achieved. On increasing the CNC content from 0% to 0.75%, dielectric breakdown strength increased from 28.5 to 32.5 MV m^{-1}. On raising the CNC content from 0% to 1%, the capacitance increased from 18.5 to 43.4 pF (i.e., a 134% increase).[183]

Micro fibrillated cellulose (MFC)/lignosulfonate hydrogels were printed and carbonized for use as electrically conductive material in lithium-ion batteries. Experimenters printed 20–50% lignosulfonate +2% MFC aqueous ink by DIW; this was dried first in the air for 5 days, and then at 110 °C or by freeze-drying. The prints were then carbonized in an argon atmosphere in a tubular oven to 800 °C at 5 °C min^{-1} and provided 5–55 S m^{-1} electrical conductivity. The material could be printed up to 40% lignosulfonate concentration but had significant shrinkage on drying for lignosulfonate concentrations above 10%.[184]

Hygroscopic salt $CaCl_2$, was incorporated in oxidized CNF (using TEMPO) to make elastic-tunable CNF because the elastic modulus of cellulose is significantly affected by water content. Experimenters printed 2–2.5% CNF by DIW at 20 and 25% infill density. The print was immersed in a $CaCl_2$ bath, frozen, and then freeze-dried. The excess $CaCl_2$ was removed by washing with water. This printed monolith could be used as an electrical-resistance-based pressure sensor due to the excellent shape recovery after compression and the presence of salt ions. Lower infill density or higher $CaCl_2$ concentration increased pressure sensitivity, outperforming composites like CNT/polyurethane and graphene/polyamide (**Figure 14a**).[185]

In another study on printed pressure sensors of CNF composites, lightweight printed conductive foams were prepared by making composites of polypyrrole conductive polymer and carboxymethylated CNF by DIW. Carboxymethylation of pulp was carried out using monochloroacetic acid and NaOH in a solvent mixture containing isopropanol, methanol, and water. This derivatized pulp was then converted to CNF by passing through an ultra-friction grinder. Sodium dodecyl sulfate (SDS) surfactant was then added to this carboxymethylated CNF and homogenized to convert the paste into foam. After DIW printing, the printed foams were soaked in aqueous ammonium persulfate and then in aqueous solution of pyrrole for polymerization. The foams

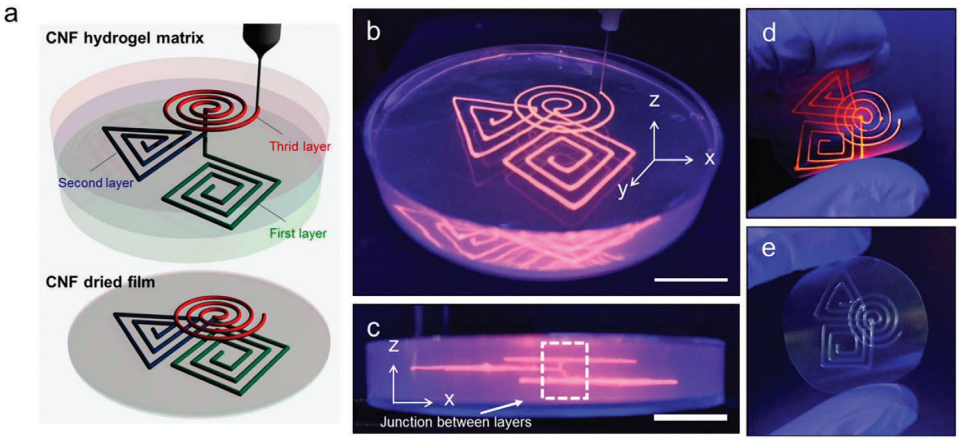

Figure 15. Fabrication of a flexible microfluidic thin film with multilayered channels by matrix-assisted 3D printing in a CNF hydrogel. a) Series of fabrication processes for three-layered continuous microfluidic channels designed by CAD. b) The nozzle tip was moved to the three layers, and the petroleum jelly-based removable ink was injected into the CNF hydrogel matrix. Ink with fluorescent dye was visualized under UV illumination. c) It was possible to interconnect the layers by continuous injection of the ink in tip movement to the next layer. d) CNF hydrogel matrix was dehydrated and formed a thin compact microfluidic film. e) Printed ink was liquefied at elevated temperature and removed under vacuum, forming an open-channel 3D microfluidic device. Adapted with permission.[187] Copyright 2017, American Chemical Society.

were then washed and dried. The lowest bulk density achieved was 18 kg m^{-3}. It was found that 0.76 g polypyrrole/g CNF had the best balance of printing quality, conductivity, and compression strength and was stable after 20 compression cycles at 20% strain (Figure 14b).[186]

Microfluidic channels were created inside the CNF matrix by using petroleum jelly because of its immiscibility and easy removal from the matrix after drying. A 0.4–1% CNF hydrogel was poured into a petri dish, and petroleum jelly was extruded using DIW, with the syringe needle inserted into the hydrogel. This process created three layers at different depths that were interconnected due to continuous extrusion throughout the printing (**Figure 15**). The hydrogels were dried, and the jelly was removed by passing compressed air and hexane through the channel. A 10% trimethylchlorosilane solution was passed through the channel to silylate the surfaces and render them hydrophobic. The silicone elastomer and curing agent in hexane were passed and cured at

80 °C to coat the inner surfaces with polymerized silicone. The microfluidic devices had diffusion-limited co-flows similar to those of conventional polydimethylsiloxane (PDMS) open-channel microfluidic devices. The device was used to show selective detection of chromium and nickel ions in wastewater by colorimetric detection using dimethylglyoxime at pH 9 for Ni^{2+} (pink) and diphenylcarbazide at pH 1 for Cr^{6+} (purple) via UV–Vis spectrophotometry.[187]

7. CNM-Based Hydrogel Scaffolds for Biomedical Applications

AM enables the design of complex structures that can replicate the original anatomical shape of an injured body part to be repaired and, in particular, mimic the native extracellular matrix depending on their composition, so that new tissue can grow within the wound. These complex structures are typically printed scaffolds made of biomaterials: that is to say, materials that are biocompatible and biodegradable, nano-cellulose is one of the key components, as it has attracted much interest for applications like tissue engineering and wound healing (including in some cases the simultaneous delivery of drugs and growth factors).[188] The scaffold synthesis process consists of three main steps: extrusion/jetting of a bioink, printing of the scaffold, and stabilization of the printed structure (by cross–linking, generally). Moreover, the hydrogel and the associated scaffold must satisfy all the different criteria listed below, which makes their use for tissue engineering a puzzle that is difficult to solve:

- The hydrogel must show homogeneity, shear thinning behavior, appropriate level of viscosity (to avoid high pressure during extrusion), and viscoelastic solid properties at low shear stress to retain shape after printing (thixotropic behavior).
- A level of mechanical performance must be achieved for the scaffold to provide the required support (for example, compression properties are important for the repair of cartilage and bone tissues). A list of the mechanical properties obtained with different nanocellulose-containing hydrogels of different compositions, as well as the related applications, can be found in **Table 1**.
- The structure of the scaffold must provide an interconnected pore structure that will enable cell migration, nutrient transport, discharge of metabolic waste, and oxygen diffusion (pores in the range of 100–600 microns).
- The surface properties of the scaffold (porosity of 10–40 microns, active surface functional groups) must be engineered to promote cell adhesion, growth, proliferation, migration, and differentiation.
- The materials involved must be non-toxic, biocompatible, and biodegradable (they should degrade without generating toxic metabolites).

To check all these criteria, most studies follow a similar evaluation process: shear rheology, mechanical testing (compression

Table 1. Hydrogel structure, mechanical properties of the corresponding scaffold, and associated medical application (Unpublished).

Refs.	Hydrogel structure/composition	Mechanical properties	Medical application
[203]	PVA (12 wt.%) hexagonal boron nitride (0.25 wt.%), bacterial cellulose (0.1 wt. %)	Tensile strength: 0.13 MPa, Elongation at break: 80%	Bone tissue engineering
[211]	Two-layer structure with each layer cross–linked by epichlorohydrin. Top layer: pure cellulose (8 wt.%) Bottom layer: cellulose+bioactive glass (10 wt.%)	Tensile strength: 5 MPa, Compressive strength: 12 MPa	Repair of cartilage and underlying bone
[191]	CNCs (6.9 wt.%), sodium alginate (1.5 wt.%), gelatin (1.5 wt.%), cross–linked by $CaCl_2$ and glutaraldehyde	Compressive modulus: 0.16–0.34 MPa	Cartilage repair
[200]	PLA printed on bacterial cellulose membrane	Tensile strength: 65 MPa	Tissue engineering and nerve repair
[201]	Porous 3D printed PLA support, Chitosan-collagen (3:1 by weight) electrospun CNF hydrogel composite deposited and cross–linked by genipin.	Compressive strength: 0.032 MPa	Cartilage repair/meniscus tissue engineering
[204]	Poly(Ɛ-caprolactone) (5 wt.%) nanocrystalline cellulose surface treated by poly(glutamic acid)	Compression modulus: 101–122 MPa, Compressive strength: 40–60 MPa	Bone tissue regeneration
[192]	Gelatin (2 wt.%), oxidized dextran (2 wt.%), and CNCs (0.4 wt.%)	Compressive strength: 1.33 MPa, Compressive modulus: 0.134 MPa	Tissue repair
[189]	Bacterial CNFs (0.7 wt.%) +gelatin/glycerol/silk (6 wt.%/62 wt.%/31 wt.% of dry product)	Compressive strength: 0.065 MPa at 30% strain, Compressive modulus: 0.187 MPa	Tissue engineering
[193]	Sodium alginate/nanoclay (0.5wt.%), ethylene-diamine-tetra-acetic acid calcium disodium salt hydrate/TEMPO-oxidized bacterial cellulose	Compression strength at 40%: 0.334 MPa, Compression modulus: 0.270 MPa	Drug release, tissue engineering
[194]	Polycaprolactone/gelatin (1:1 by weight) and bacterial cellulose (0.25 wt.%)	Tensile strength: 2.17 MPa	Bone tissue engineering
[195]	CNCs/sodium alginate/gelatin (70/20/10 wt.%)	Tensile modulus: 1.54 MPa, Tensile strength: 0.021 MPa in wet conditions.	Tissue regeneration
[198]	Calcium phosphate/calcium sulfate hemihydrate (2:3 ratio by weight, for a total of 20 wt.%)/alginate wt.%/hydroxypropyl methylcellulose 0.9 wt.% and cross–linked in $CaCl_2$	Compressive modulus: 56 MPa, Compressive strength: 13 MPa	Non-load-bearing bone tissue regeneration
[196]	TEMPO-oxidized cellulose nanofibrils (0.9 wt.%) + gelatin methacrylate (1 wt.%). Cross–linked by Ca^{2+} ions and by ultraviolet (photoinitiator Irgacure 2959 at 0.5 wt.%)	Compressive modulus: 0.0014–0.004 MPa	Wound healing
[213]	Poly-lactic-co-glycolic acid (85 lactide:15 glycolide by weight), polyethylene glycol (93.5:6.5 ratio by weight) blend added to water and carboxymethyl cellulose (0.1 to 4 wt.%) to form a paste (solids ratio 1:1 to 1.7:1 by weight)), extruded and sintered at 37 °C and immersed in NaCl (0.9 wt.%).	Compressive modulus: 54–57 MPa, Compressive yield strength: 1.15–1.22 MPa	Bone repair

test, eventually tension test), electronic microscopy to characterize the pore structure, Fourier transform IR spectroscopy to investigate the composition, and in-vitro and in-vivo studies to evaluate biocompatibility, bioactivity, and biodegradation. Some of the mentioned processes of scaffold synthesis and testing are depicted in **Figure 16**.

The majority of bioinks consist of naturally derived polymer-based hydrogels, which are made of water in the majority, and of hydrophilic biopolymers that have the ability to retain large quantities of that water. This makes the bioinks structurally similar to the extracellular matrix to be mimicked. The main biopolymers are gelatin,[189–196] alginate,[190, 191, 193, 195, 197–199] PLA,[200–202] chitosan[201] and modified chitosan,[197] collagen,[201] oxidized dextran,[192] and silk.[189] Not bio-sourced but biodegradable polymers have also been used, like polyvinyl alcohol[203] and polycaprolactone (not in hydrogel form).[204]

The mechanical properties of pure hydrogels are too poor to provide the required support during wound healing, and so different strategies to improve them have been investigated. These strategies can be separated between pre-printing and post-printing methods. The pre-printing methods consist of adding nanoparticles to the hydrogel. Among these, three types of nanocellulose (cellulose nanocrystals, cellulose nanofibrils, and bacterial cellulose) have been used. Nanocellulose is a good hydrogel filler for biomedical applications because it is biocompatible, has low toxicity, a high specific surface area, high mechanical properties, and is renewable. Also, the high concentration of hydroxyl groups in cellulose provides some hydrophilicity that participates in the retention of water in the hydrogel and offers anchorage for the grafting of tailored functional groups that will generate a strong interaction with the biopolymer. As discussed in previous sections, CNCs with rod-like morphologies, high tensile properties (modulus of 150 GPa and strength of ≈7–8 GPa),

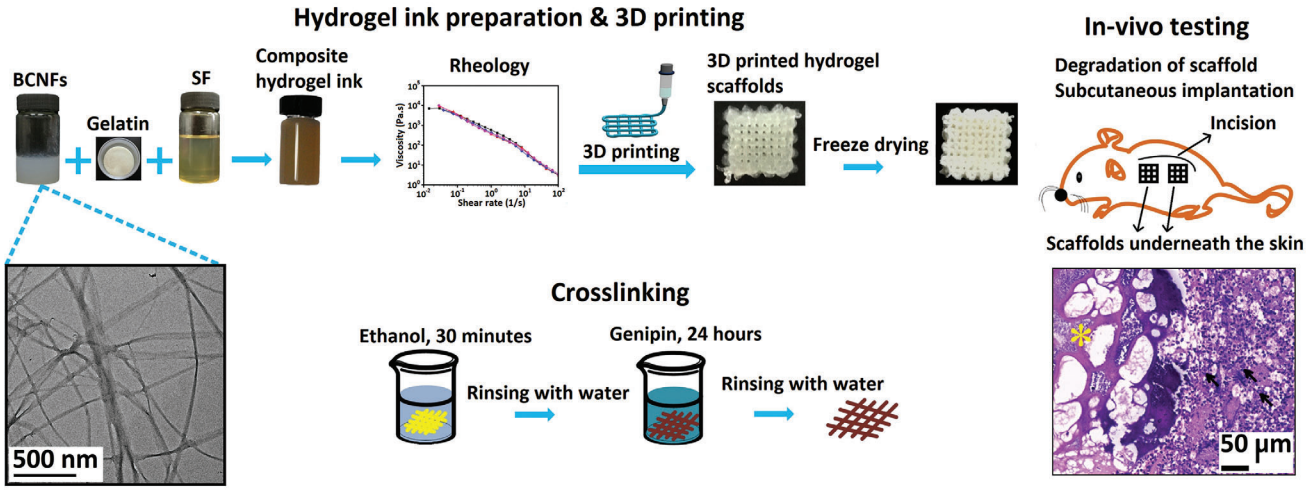

Figure 16. Development and testing processes of a 3D printed hydrogel scaffold (gelatin + silk + glycerol + genipin + bacterial cellulose nanofibers). Adapted with permission.[189] Copyright 1981, PERGAMON, Elsevier.

and thermal stability up to 300 °C,[188] are particularly adapted to 3D printing because they confer a shear thinning behavior to the hydrogel. CNFs are comparatively more flexible than CNCs, with a tensile strength of 1–3 GPa,[188] and their complex structural design mimics the native extracellular matrix more closely than CNCs. Bacterial nanocellulose is in the form of nanofibrils (25 nm in diameter), which agglomerate into 100 nm-wide ribbons[188] and are produced by some bacteria. The fibrils have a high degree of purity and crystallinity, have high mechanical strength, can be used as is (without extra purification steps to remove lignin and hemicellulose, as opposed to CNFs and CNCs), and can be easily molded into different shapes.[194,205,206] For each type of nanocellulose, the quality of dispersion and interaction with the surrounding water and biopolymer depend on a controlled modification of the hydroxyl groups. Adding a second filler to improve the scaffold's mechanical properties was evaluated. For example, boron nitride nanoplatelets were added to compensate for a decrease in tensile properties after the incorporation of bacterial cellulose in PVA.[202]

Post-printing methods to improve the mechanical properties of the printed scaffold include the removal of some of the water to increase the concentration of cellulose particles and the density of hydrogen bonds between the hydroxyl groups. This can be done by wet densification, during which a solvent such as ethanol, acetone, or acetonitrile is added to the hydrogel.[141] Further water removal can be achieved using freeze-drying.[189,193,201,207,208] Ionic interactions can be generated between some divalent cations such as calcium ion (Ca^{2+}) and the biopolymer, like in the case of alginate,[141,190,193,195,197–199,209] or between the cation and the CNPs.[196] This is typically achieved by dipping the scaffold in a solution containing the cation. Ionic interactions can also exist between the cellulose particles and the biopolymer.[196] Cross–linking of the scaffold can be the result of several covalent bonding interactions such as i) matrix-matrix: alginate and gelatin,[195] carboxymethyl cellulose and citric acid,[207] ii) matrix-cross-linker: gelatin with glutaraldehyde,[191] or genipin[120–132,189–201] or oxidized dextran,[192] iii) matrix-additives/plasticizers: silk and glycerol.[189] Photopolymerization with UV light was also used to cross–link methacrylated gelatin,[196] poly-lactic-co-glycolic acid with polyethylene glycol,[208,209] methacrylated PLA particles with methacrylated nanocrystalline cellulose,[202] or methacrylated carboxymethyl cellulose.[210] Cellulose can also be cross–linked by epichlorohydrin to form a percolating network.[211]

The interconnected pore structure is mainly defined by the printing parameters, with some influence coming from the expansion or shrinking of the hydrogel due to intramolecular interactions,[192] potential cross–linking,[192] freeze-drying,[201,208] cryogelation,[202] or wet densification, and the presence of fillers like cellulose nanocrystals.[192,208] The level of porosity also has a direct influence on the mechanical performance of the printed scaffold.

Small porosity at the surface of the scaffold can be typically created by the freeze-drying process.[189,207,208] Some surface topography can also be related to the filler.[194,195,198,212] It was observed that the topography of the scaffold surface at a nanometer range was responsible for cell adhesion,[195,198,201] growth,[195,201] proliferation,[195,196,198] migration,[201] and phenotype change.[201,212] It was shown that the addition of cellulose nanocrystals to an alginate+gelatin hydrogel improved the hydrophilicity of the scaffold surface, which led to better cell adhesion and bone growth.[190] Cellulose nanofibrils had a positive impact on cell viability.[199] The addition of bacterial cellulose was responsible for improved cell adhesion on a PVA-based scaffold.[203] Nanoclay particles added as a second filler induced specific interactions with adjacent cells and promoted their proliferation.[193] Surface treating cellulose with poly (glutamic acid) and with adhered stem cells led to the growth of bone tissue around a polycaprolactone-based scaffold.[204] Using methacrylate gelatin created some specific interactions that improved cell adhesion (in the case of fibroplasts[196]). Also, incorporating bioactive additives in a hydrogel containing nanocellulose could promote tissue regeneration. The loading of platelet-rich plasma in the scaffold helped with the healing of diabetic wounds.[207] Hydroxyapatite enhanced cell viability.[194] Adding particles of bioglass promoted collagen production.[141] It was even reported that AM of a hydrogel containing living cells (stem

cells,[199] human nasoseptal chondrocytes,[209] or primary human mesenchymal cells[213]) did not significantly reduce cell viability. Incorporating these cells in the hydrogel helped with faster tissue growth and wound healing. Encapsulated proteins can tolerate the mixing and extrusion process associated with 3D printing as well, and it was demonstrated that they could help with tissue development and repair.[213]

8. Concluding Remarks and Future Perspectives

CNMs are highly promising for AM applications thanks to their large surface area, biodegradability, and superior mechanical properties, as discussed in this review. However, there are several challenges that must be overcome before these materials can be adopted on an industrial scale, including CNM agglomeration and their dispersion in thermoplastic polymer matrices while preserving their nanofibrillar structure. Our review summarizes past and ongoing efforts on the production and dispersion of CNMs into polymers, AM processes, and applications of 3D-printed CNM-based composites.

As discussed here, CNMs, especially CNFs, are mostly produced via mechanical fibrillation in water. Due to the extremely high viscosity of CNF-water suspensions, they are produced at a significantly high water content (97 wt.%). Therefore, they need to be dewatered (dried) prior to incorporation into polymers, which is extremely energy-intensive due to this very high-water content. Furthermore, due to rich OH groups on the surface, they irreversibly agglomerate, losing their nano-fibrillar structure upon drying via conventional methods, which nullifies the whole fibrillation process. The presence of strong inter-CNF interactions due to hydrogen bonding further leads to their aggregation in polymer matrices used for 3D printed nanocomposites which are mostly hydrophobic albeit a few. Both experimental and modeling studies have focused on addressing each of these specific challenges for utilizing CNM-based materials across different manufacturing techniques and applications. In this review, we provided an overview of the implications of these independent findings in the context of AM and how a combined multi-scale modeling method and experimental approach would benefit the rapid discovery and optimization of materials and AM processes for CNM-based nanocomposites.

The fundamental water organization around CNMs, competitive cellulose-cellulose versus cellulose-solvent interactions, and thermodynamic barriers to aggregation and dispersion were provided by experiments (NMR, DSC) and MD simulations. Co-solvents and CNM surface modifications have also been identified to overcome CNM aggregation for use as an AM feedstock. CNM chains where the exposed C6 hydroxyl groups are modified to contain charged moieties (COO^-, $OSO3^-$) or functional groups with increased hydrophobicity ($OCOCH_3$) were shown to reduce inter-CNM interactions and improve dispersion. A rational choice of co-solvents systems to reduce CNM aggregation is suggested: moderately polar aprotic solvents (such as THF-H_2O, GVL-H_2O), or a mixture of hydrogen bond donors and acceptors (such as NaOH/urea/water, glycerol/water, acetone-water) are expected to engage different cellulose surfaces and reduce inter-fiber interactions. The NaOH-urea-water system containing a strong base, and a small organic molecule acting as a hydrogen-bond acceptor/donor reduced the inter-fibril contacts in a CNF (CNC) bundle and led to a ≈21% reduction in fibrillation energy. CG simulations have played a pivotal role in understanding CNM conformational dynamics in solution and predicting aggregation behavior on a microsecond timescale significantly reducing computational costs. While design principles have been derived from the current modeling-experimental fibrillation studies, an integrated approach can be exploited for large-scale, accelerated solvent screening for CNM dispersion. All-atom and CG MD-computed quantities such as inter-fibril/inter-CNF contacts and energies ($\Delta G/\Delta E$) can be combined with thermodynamic models to predict solvents with better physicochemical properties (high solubility, viscosity, surface tension, hydrogen bond donor/acceptor capabilities). Inter-fibril/inter-CNM contacts, and energetics, can be correlated with solvent features and subsequently used to train machine learning models to predict solvents that improve CNM dispersion. The following factors must be considered to perform high-throughput accurate MD calculations in solvents: 1) selection of a representative CNM-solvent system – 18- versus 36-chain nanofibrils, bundle sizes (4–7 nanofibrils), and solvent concentration 2) appropriate choice of atomistic forcefield parameters and optimization of CG solvent-solvent and CNM-solvent interaction parameters as needed, 3) choice of method to compute contacts and energies – sampling time, free energy method, collective variables and convergence criteria. Besides the high-throughput approach, future multi-CNC/CNF (multiple 7-fibril bundles) MD simulations in target solvents will provide insight into the thermodynamic and kinetic barriers to CNM aggregation as well as elucidate long-timescale aggregation dynamics. A potential future direction is to first perform simulations with multiple CNF/CNC bundles in solvents focusing on the crystalline part, which can then be followed by incorporating amorphous fragments; this approach could avoid the complexities and challenges in sampling the heterogeneities. A combined high-throughput pipeline involving modeling and fibrillation experiments is expected to improve the dispersion of CNMs to facilitate their use as a feedstock in AM.

The optimization of both materials (polymer and CNM surface modifications/additives) and processes for AM of nanocomposites on a large-scale is cumbersome as it involves laborious experimental trial-and-error. While the methods for addressing challenges associated with obtaining dispersed CNMs as AM feedstocks are discussed above, improving matrix-filler interfacial compatibility and mechanical strength can be achieved by combining multi-scale modeling (all-atom, CG, and FEM) methods with pilot-scale 3D printing experiments. As discussed in the review, all-atom and CG MD simulations have been used to identify interactions between the native/surface-modified CNM and polymer functional groups, morphology, work of interfacial adhesion, tensile stress–strain curves, and the accompanying changes in morphologies. While MD simulations provide predicted material properties and an understanding of the fundamental interactions and energetics, they do not directly address the physical challenges with the AM process itself. Further, even ultra coarse-grained simulations cannot capture properties and structural phenomena closer to macroscopic time scales such as aging, creep behavior, and defect formation including void and crack propagation and growth on a large length scale (a few micrometers to millimeters). The majority of the printing methods covered in this review are extrusion-based methods, either melt

extrusion deposition or DIW. It is important to note that while CNMs are utilized to improve rheology and final part properties in many cases, their role as an enabler in the AM process is perhaps more critical, especially in melt extrusion-based processes. The addition of cellulose fibers does not only improve rheology, and increase zero-shear viscosity and yield stress, but it also minimizes warpage/distortion of the part due to residual stress buildup by improving thermal expansion and contraction behavior and the stiffness of the material. Especially in large-scale AM, it is almost impossible to print large parts using neat-polymer resins: that is why fibers, such as carbon, cellulose, or glass fibers, are added into the polymer feedstock. Nanoparticles can act as nucleation points and promote crystallization, which in return can impact the printing process negatively, creating further residual stress buildup. Optimizing the printing parameters and hybridizing CNMs with larger-scale cellulose fibers has been shown to overcome these issues.[136] Using CNMs and other cellulose-based fibers as enablers in these processes eliminates the need to use other high embodied energy, high-carbon-footprint fibers and fillers such as carbon and glass fibers. Relative to these non-bio-based fibers and fillers, CNMs have considerable environmental benefits, including being biodegradable, non-toxic, renewable, and less energy-intensive during production.[9] Continuum models, specifically FEA, are highly valuable in predicting and optimizing parameters for the whole AM process. It can further evaluate long-timescale mechanical, thermal, and transport properties of nanocomposites. As described here, the majority of the AM processes covered in this study include material extrusion, deposition, and retention of shape (i.e., preventing distortion) and geometrical accuracy. The material system, dispersion level, solids loading, glass transition temperature, crystallization temperature, as well as processing variables like bed temperature or cooling rate (in AM, this would be related to layer time, distance from the print head, etc.) all impact the whole printing process and final part properties. Therefore, developing FEA models that can predict the temperature profiles and distortion behavior of different CNM–polymer material formulations at different printing conditions will be extremely helpful in AM process optimization. As an example of FEA AM process modeling, Kim et al.[214–216] reported a study on large-scale AM of carbon fiber–ABS composites. Their work focused on measuring the fundamental thermal and mechanical properties of 3D-printed material in all three directions (x, y, z) due to anisotropy. They incorporated that information into an FEA model to predict the temperature profile during the printing process and then the distortion behavior of the final printed part at different printing parameters. This allowed toolpath optimization to minimize the residual stress buildup and distortion controlling the printing parameters, as well as, to some extent, the temperature profile. Although this work focused on micro-scale cellulose fibers, there are FEA studies effectively predicting the viscoelastic properties of cellulose nanofiber-based composites,[128–133] and the study above can be extended to include CNM composites allowing printing process optimization, and especially toolpath optimization.

For high-throughput manufacturing of CNM-polymer nanocomposites, we discussed an integrated multi-scale modeling-experimental approach where material properties would be provided as inputs from MD simulations to the FEM module. Input properties include but are not limited to bulk density, polymer-filler composition, Young's modulus, viscosity, heat capacities, glass transition temperatures, and matrix relaxation time. Screened candidates with optimal properties from MD simulations and FEM predictions along with the associated AM process parameters will then be prioritized for pilot-scale experiments. There are several challenges that need to be overcome to ensure the implementation and success of this pipeline. While coarse-grained forcefields exist for cellulose and some thermoplastic polymers, they need to be carefully validated against the available literature data. For predicted Young's modulus, we note the strain rate could be relatively higher in MD simulations than in experiments, requiring a scaling factor if needed for a direct comparison with experiments. The microstructure can greatly impact the melt rheology as well as the reinforcing mechanism. For example, in the work of Tekinalp et al.,[171] freeze-dried CNFs were found in bundles rather than individual fibers, and the hydrogen bonding holding these fibrils together as a bundle acted as a part of the reinforcing mechanism, allowing the polymer to penetrate within the bundle and creating mechanical interlocking. Such effects must be considered in future nanocomposite simulations. As in the case of MD simulations with solvents, to accelerate the process, MD-computed properties for a representative CNM-polymer system (interfacial adhesion, contacts) can be combined with the literature data/database for matrix polymer properties[134,217] to provide material properties for promising candidates to the FEM models.

As discussed in this review, CNMs are well-known rheology modifiers, even at small concentrations, and in the development of AM feedstocks these materials have been shown to significantly increase the viscosity of polymer melts and to change their rheological behavior.[165] The role of CNMs as a rheology modifier has not been limited to only thermoplastic composites, which are required to be melted to flow: they have also been used in many unique applications to modify the rheology of liquid resins to convert them into 3D printable inks for the DIW process. In addition to improving viscoelastic behavior for better printability and dimensional stability in some applications, such as printed scaffolds, CNCs have been utilized to improve electric properties, such as the dielectric constant and capacitance, in printed electronics applications. Similarly, in other DIW studies, carboxymethylated CNFs have been utilized along with a conductive polymer to print conductive foams for pressure sensor application, while CNCs have been added into a hydrogel to improve the hydrophilicity of the scaffold surface, which led to better cell adhesion and bone growth. We further identified a few target applications where our design principle and pipeline can be applied to improve the AM process. CNMs have been utilized in many different extrusion-based AM applications, either improving or enabling the printing process, improving final printed part properties, or adding additional functionality. Although they offer many benefits both in terms of processability and performance, the challenges to manufacture, dry, and incorporate them into matrix materials remain and limit their wider industrial adoption—especially in scaled-up applications. Although most of the MD and FEA simulation studies are specific to certain material systems and compositions, they provide great overall guidance from the manufacturing of the CNMs to the printing process and final composite properties. Similarly, many different applications of

3D-printed CNMs from electronics to biomedical applications, from packaging to structural applications, have been reported. While more research needs to be conducted to expand the scope of these studies and cover wider material systems, they are all promising and demonstrate the great potential of CNMs in AM and many different applications. Furthermore, other applications not included in this review due to our focus on AM may dramatically speed up the adoption of the use of CNMs in composite and AM applications. These include studies focusing on altering the surface chemistry of CNMs to facilitate easier drying and better polymer matrix interaction via lowering their hydrophilicity; the development of low-water or waterless fibrillation approaches; and innovative drying technologies that can eliminate/minimize agglomeration. With all these improvements, and unlike other nanomaterials, CNMs, and especially CNFs, are targeted to be available at commodity prices (i.e., <$5 lb^{-1}) and thus accommodate wide industrial adoption.

Acknowledgements

S.D. and S.J.R. contributed equally to this work. This review is based upon work supported by the US Department of Energy (DOE), Office of Energy Efficiency and Renewable Energy, Advanced Materials and Manufacturing Office (AMMTO), Oak Ridge National Laboratory/University of Maine SM^2ART program with research and resources used at the Manufacturing Demonstration Facility (MDF), a DOE AMMTO User Facility, and the Advanced Structures and Composites Center (ASCC), a University of Maine research center under CPS Agreements 35714 and 38563, the Bioenergy Technologies Office (BETO), the Oak Ridge Leadership Computing Facility, a DOE Office of Science User Facility, Johnson & Johnson WiSTEM2D Scholars Award, Moore Inventor Fellow award, and American Chemical Society PRF award 66747-ND7. The authors thank Dr. Shih-Hsien Liu for his input on co-solvent screening through combined MD simulations and experiments to reduce CNF fibrillation energy.

Conflict of Interest

The authors declare no conflict of interest.

Keywords

additive manufacturing, composites, fibrillation, finite element modeling, molecular dynamics, nanocellulose

Received: August 5, 2024
Revised: October 21, 2024
Published online:

[1] S. Bhagia, K. Bornani, R. Agrawal, A. Satlewal, J. Ďurkovič, R. Lagaňa, M. Bhagia, C. G. Yoo, X. Zhao, V. Kunc, Y. Pu, S. Ozcan, A. J. Ragauskas, *Appl. Mater. Today* **2021**, *24*, 101078.
[2] X. Zhao, H. Tekinalp, X. Meng, D. Ker, B. Benson, Y. Pu, A. J. Ragauskas, Y. Wang, K. Li, E. Webb, D. J. Gardner, J. Anderson, S. Ozcan, *ACS Appl. Bio Mater.* **2019**, *2*, 4557.
[3] P. A. G. S. Giachini, S. S. Gupta, W. Wang, D. Wood, M. Yunusa, E. Baharlou, M. Sitti, A. Menges, *Sci. Adv.* **2020**, *6*, eaay0929.
[4] S. Bhagia, S. Kore, S. Wasti, J. Ďurkovič, J. Kováč, X. Zhao, H. B. Andrews, M. Martin, N. C. Gallego, U. Vaidya, S. Ozcan, *Polym. Test.* **2023**, *118*, 107916.
[5] H. Tetik, K. Zhao, N. Shah, D. Lin, *J. Manuf. Process.* **2021**, *68*, 445.
[6] M. L. Rencheck, M. Korey, X. Zhao, H. Tekinalp, S. Ozcan, *Mater. Today Commun.* **2023**, *34*, 105525.
[7] M. Korey, M. L. Rencheck, H. Tekinalp, S. Wasti, P. Wang, S. Bhagia, R. Walker, T. Smith, X. Zhao, M. E. Lamm, K. Copenhaver, U. Vaidya, S. Ozcan, *Composit. Part B* **2023**, *256*, 110652.
[8] A. Kulachenko, T. Denoyelle, S. Galland, S. B. Lindström, *Celllulose* **2012**, *19*, 793.
[9] L. Wang, P. V. Kelly, N. Ozveren, X. Zhang, M. Korey, C. Chen, K. Li, S. Bhandari, H. Tekinalp, X. Zhao, J. Wang, M. Ö. Seydibeyoğlu, E. Alyamac-Seydibeyoglu, W. M. Gramlich, M. Tajvidi, E. Webb, S. Ozcan, D. J. Gardner, *Matter* **2023**, *6*, 344.
[10] V. Ganapathy, G. Muthukumaran, P. E. Sudhagar, A. Rashedi, M. N. F. Norrrahim, R. A. Ilyas, K. L. Goh, M. Jawaid, J. Naveen, *Polym. Compos.* **2023**, *44*, 734.
[11] R. Rusli, S. J. Eichhorn, *Appl. Phys. Lett.* **2008**, *93*, 033111.
[12] *Kevlar Aramid Fiber: Technical Guide. Dupont*, https://www.dupont.com/content/dam/dupont/amer/us/en/safety/public/documents/en/Kevlar_Technical_Guide_0319.pdf, (accessed: June 2024).
[13] A. Dufresne, *Mater. Today* **2013**, *16*, 220.
[14] A. Dufresne, *Nanocellulose: From Nature to High Performance Tailored Materials*, De Gruyter, Berlin, Boston **2017**.
[15] J. Lemaitre, J. L. Chaboche, A. Benallal, R. Desmorat, in *Mécanique des matériaux solides*, 3e Ed, Dunod, France **2020**.
[16] X. Zhao, S. Bhagia, D. Gomez-Maldonado, X. Tang, S. Wasti, S. Lu, S. Zhang, M. Parit, M. L. Rencheck, M. Korey, H. Jiang, J. Zhu, X. Meng, M. E. Lamm, K. Copenhaver, M. S. Peresin, L. Wang, H. Tekinalp, G. Yang, V. Kumar, G. Chen, K. Nawaz, X. Chelsea Chen, U. Vaidya, A. J. Ragauskas, E. Webb, D. J. Gardner, P. He, X. He, K. Li, et al., *Mater. Today* **2023**, *66*, 409.
[17] M. E. Lamm, K. Li, D. Ker, X. Zhao, H. E. Hinton, K. Copenhaver, H. Tekinalp, S. Ozcan, *Cellulose* **2022**, *29*, 3859.
[18] K. Li, D. Mcgrady, X. Zhao, D. Ker, H. Tekinalp, X. He, J. Qu, T. Aytug, E. Cakmak, J. Phipps, S. Ireland, V. Kunc, S. Ozcan, *Carbohydr. Polym.* **2021**, *256*, 117525.
[19] N. B. Palaganas, J. D. Mangadlao, A. C. C. de Leon, J. O. Palaganas, K. D. Pangilinan, Y. J. Lee, R. C. Advincula, *ACS Appl. Mater. Interfaces* **2017**, *9*, 34314.
[20] W. T. Le, A. Kankkunen, O. J. Rojas, M. R. Yazdani, *Sol. Energy Mater. Sol. Cells* **2023**, *256*, 112337.
[21] K. Copenhaver, K. Li, M. E. Lamm, C. Walker, D. Johnson, Y. Han, L. Wang, X. Zhao, Y. Pu, H. Hinton, H. Tekinalp, S. Bhagia, A. J. Ragauskas, D. J. Gardner, S. Ozcan, *ACS Sustainable Chem. Eng.* **2021**, *9*, 13460.
[22] K. Copenhaver, K. Li, L. Wang, M. Lamm, X. Zhao, M. Korey, D. Neivandt, B. Dixon, S. Sultana, P. Kelly, W. M. Gramlich, H. Tekinalp, D. J. Gardner, S. MacKay, K. Nawaz, S. Ozcan, *Cellulose* **2022**, *29*, 4835.
[23] L. Wang, D. J. Gardner, J. Wang, Y. Yang, H. L. Tekinalp, M. Tajvidi, K. Li, X. Zhao, D. J. Neivandt, Y. Han, S. Ozcan, J. Anderson, *Compos. B Eng.* **2020**, *201*, 108297.
[24] L. Wang, K. Li, K. Copenhaver, S. Mackay, M. E. Lamm, X. Zhao, B. Dixon, J. Wang, Y. Han, D. Neivandt, D. A. Johnson, C. C. Walker, S. Ozcan, D. J. Gardner, *Biomacromolecules* **2021**, *22*, 4037.
[25] Q. Wang, J. Sun, Q. Yao, C. Ji, J. Liu, Q. Zhu, *Cellulose* **2018**, *25*, 4275.
[26] D. Plackett, M. Iotti, in *Biopolymer Nanocomposites*, John Wiley & Sons, Inc., Hoboken, NJ, USA **2013**, pp. 309-338.
[27] G. Siqueira, J. Bras, A. Dufresne, *Biomacromolecules* **2009**, *10*, 425.
[28] S. Y. Ding, S. Zhao, Y. Zeng, *Cellulose* **2014**, *21*, 863.
[29] J. D. Kubicki, H. Yang, D. Sawada, H. O'Neill, D. Oehme, D. Cosgrove, *Sci. Rep.* **2018**, *8*, 13983.

[30] B. T. Nixon, K. Mansouri, A. Singh, J. Du, J. K. Davis, J. G. Lee, E. Slabaugh, V. G. Vandavasi, H. O'Neill, E. M. Roberts, A. W. Roberts, Y. G. Yingling, C. H. Haigler, *Sci. Rep.* **2016**, *6*, 28696.
[31] Y. Nishiyama, *Philos. Trans. A Math. Phys. Eng. Sci.* **2018**, *376*, 201700472.
[32] M. Wohlert, T. Benselfelt, L. Wågberg, I. Furó, L. A. Berglund, J. Wohlert, *Cellulose* **2022**, *29*, 1.
[33] I. Sakurada, Y. Nukushina, T. Ito, *J. Polym. Sci.* **1962**, *57*, 651.
[34] F. Tanaka, T. Iwata, *Cellulose* **2006**, *13*, 509.
[35] X. Xu, F. Liu, L. Jiang, J. Y. Zhu, D. Haagenson, D. P. Wiesenborn, *ACS Appl. Mater. Interfaces* **2013**, *5*, 2999.
[36] X. Wu, R. J. Moon, A. Martini, *Cellulose* **2013**, *20*, 43.
[37] C. Djahedi, L. A. Berglund, J. Wohlert, *Carbohydr. Polym.* **2015**, *130*, 175.
[38] P. Chen, Y. Nishiyama, J. Wohlert, *Cellulose* **2021**, *28*, 10777.
[39] K. Nakamura, T. Hatakeyama, H. Hatakeyama, *Text. Res. J.* **1981**, *51*, 607.
[40] E. L. Lindh, C. Terenzi, L. Salmén, I. Furó, *Phys. Chem. Chem. Phys.* **2017**, *19*, 4360.
[41] L. Solhi, V. Guccini, K. Heise, I. Solala, E. Niinivaara, W. Xu, K. Mihhels, M. Kröger, Z. Meng, J. Wohlert, H. Tao, E. D. Cranston, E. Kontturi, *Chem. Rev.* **2023**, *123*, 1925.
[42] N. Barrios, J. G. Parra, R. A. Venditti, L. Pal, *Carbohydr. Polym.* **2024**, *329*, 121799.
[43] M. Norgren, C. Costa, L. Alves, A. Eivazi, C. Dahlström, I. Svanedal, H. Edlund, B. Medronho, *Molecules* **2023**, *28*, 4216.
[44] X. Falourd, C. Rondeau-Mouro, M. Cambert, M. Lahaye, B. Chabbert, V. Aguié-Béghin, *Carbohydr. Polym.* **2024**, *326*, 121579.
[45] A. S. Sridhar, L. A. Berglund, J. Wohlert, *Cellulose* **2023**, *30*, 8089.
[46] E. L. Lindh, L. Salmén, *Cellulose* **2017**, *24*, 21.
[47] E. L. Lindh, M. Bergenstråhle-Wohlert, C. Terenzi, L. Salmén, I. Furó, *Carbohydr. Res.* **2016**, *434*, 136.
[48] S. Väisänen, R. Pönni, A. Hämäläinen, T. Vuorinen, *Cellulose* **2018**, *25*, 6923.
[49] Y. Nishiyama, U. J. Kim, D. Y. Kim, K. S. Katsumata, R. P. May, P. Langan, *Biomacromolecules* **2003**, *4*, 1013.
[50] P. Langan, L. Petridis, H. M. O'Neill, S. V. Pingali, M. Foston, Y. Nishiyama, R. Schulz, B. Lindner, B. L. Hanson, S. Harton, W. T. Heller, V. Urban, B. R. Evans, S. Gnanakaran, A. J. Ragauskas, J. C. Smith, B. H. Davison, *Green Chem.* **2014**, *16*, 63.
[51] A. Chami Khazraji, S. Robert, *J. Nanomater.* **2013**, *2013*, 745979.
[52] W. Chen, G. C. Lickfield, C. Q. Yang, *Polymer* **2004**, *45*, 7357.
[53] O. Guvench, S. S. Mallajosyula, E. P. Raman, E. Hatcher, K. Vanommeslaeghe, T. J. Foster, F. W. Jamison 2nd, A. D. Mackerell Jr, *J. Chem. Theory Comput.* **2011**, *7*, 3162.
[54] K. N. Kirschner, A. B. Yongye, S. M. Tschampel, J. González-Outeiriño, C. R. Daniels, B. L. Foley, R. J. Woods, *J. Comput. Chem.* **2008**, *29*, 622.
[55] H. Yang, T. Wang, D. Oehme, L. Petridis, M. Hong, J. D. Kubicki, *Cellulose* **2018**, *25*, 23.
[56] O. E. Shklyaev, J. D. Kubicki, H. D. Watts, V. H. Crespi, *Cellulose* **2014**, *21*, 3979.
[57] J. D. Kubicki, H. D. Watts, Z. Zhao, L. Zhong, *Cellulose* **2014**, *21*, 909.
[58] H. Hosseini, S. M. Mousavi, F. R. Wurm, V. Goodarzi, *Eur. Polym. J.* **2021**, *146*, 110251.
[59] I. Sahalianov, M. G. Say, O. S. Abdullaeva, F. Ahmed, E. Glowacki, I. Engquist, M. Berggren, I. Zozoulenko, *ACS Appl. Energy Mater.* **2021**, *4*, 8629.
[60] R. Del Olmo, M. Forsyth, N. Casado, In *Adv. Nanocomposite Mater. Environ. Energy Harvest. App.* (Eds.: A. E. Shalan, A. S. Amdy Makhlouf, S. Lancaros Mendez), Springer International Publishing, Cham, **2022**, pp. 493–532.
[61] P. Chen, J. Wohlert, L. Berglund, I. Furó, *J. Phys. Chem. Lett.* **2022**, *13*, 5424.
[62] L. Petridis, J. C. Smith, *Nat. Rev. Chem.* **2018**, *2*, 382.
[63] A. Paajanen, S. Ceccherini, T. Maloney, J. A. Ketoja, *Cellulose* **2019**, *26*, 5877.
[64] M. Garg, M. Linares, I. Zozoulenko, *Biomacromolecules* **2020**, *21*, 3069.
[65] R. Sinko, S. Keten, *Appl. Phys. Lett.* **2014**, *105*, 243702.
[66] P. Chen, C. Terenzi, I. Furó, L. A. Berglund, J. Wohlert, *Macromolecules* **2019**, *52*, 7278.
[67] Y. Ogawa, Y. Nishiyama, K. Mazeau, *Cellulose* **2020**, *27*, 9779.
[68] P. Chen, G. Lo Re, L. A. Berglund, J. Wohlert, *J. Mater. Chem. A Mater. Energy Sustain.* **2020**, *8*, 23617.
[69] A. Paajanen, Y. Sonavane, D. Ignasiak, J. A. Ketoja, T. Maloney, S. Paavilainen, *Cellulose* **2016**, *23*, 3449.
[70] A. D. Glova, S. G. Falkovich, S. V. Larin, D. A. Mezhenskaia, N. V. Lukasheva, V. M. Nazarychev, D. A. Tolmachev, A. A. Mercurieva, J. M. Kenny, S. V. Lyulin, *Polym. Int.* **2016**, *65*, 892.
[71] N. B. Möttönen, A. J. Karttunen, *Molecules* **2023**, *28*, 1115.
[72] A. Peterson, A. Y. Mehandzhiyski, L. Svenningsson, A. Ziolkowska, R. Kádár, A. Lund, L. Sandblad, L. Evenäs, G. Lo Re, I. Zozoulenko, C. Müller, *Macromolecules* **2021**, *54*, 3507.
[73] Z. Ren, R. Guo, X. Zhou, H. Bi, X. Jia, M. Xu, J. Wang, L. Cai, Z. Huang, *RSC Adv.* **2021**, *11*, 19967.
[74] Z. Ren, R. Guo, H. Bi, X. Jia, M. Xu, L. Cai, *ACS Appl. Mater. Interfaces* **2020**, *12*, 3236.
[75] X. Qin, W. Xia, R. Sinko, S. Keten, *Nano Lett.* **2015**, *15*, 6738.
[76] C. A. López, G. Bellesia, A. Redondo, P. Langan, S. P. S. Chundawat, B. E. Dale, S. J. Marrink, S. Gnanakaran, *J. Phys. Chem. B* **2015**, *119*, 465.
[77] F. Grünewald, M. H. Punt, E. E. Jefferys, P. A. Vainikka, M. König, V. Virtanen, T. A. Meyer, W. Pezeshkian, A. J. Gormley, M. Karonen, M. S. P. Sansom, P. C. T. Souza, S. J. Marrink, *J. Chem. Theory Comput.* **2022**, *18*, 7555.
[78] R. A. Moreira, S. A. L. Weber, A. B. Poma, *Molecules* **2022**, *27*, 976.
[79] J. Pang, A. Y. Mehandzhiyski, I. Zozoulenko, *Cellulose* **2022**, *29*, 9493.
[80] V. Lutsyk, P. Wolski, W. Plazinski, *J. Chem. Theory Comput.* **2022**, *18*, 5089.
[81] Z. Wu, D. J. Beltran-Villegas, A. Jayaraman, *J. Chem. Theory Comput.* **2020**, *16*, 4599.
[82] U. Ray, Z. Pang, T. Li, *Cellulose* **2021**, *28*, 3359.
[83] A. Y. Mehandzhiyski, N. Rolland, M. Garg, J. Wohlert, M. Linares, I. Zozoulenko, *Cellulose* **2020**, *27*, 4221.
[84] N. Rolland, A. Y. Mehandzhiyski, M. Garg, M. Linares, I. V. Zozoulenko, *J. Chem. Theory Comput.* **2020**, *16*, 3699.
[85] A. Y. Mehandzhiyski, I. Zozoulenko, *Polysaccharides* **2021**, *2*, 257.
[86] A. Y. Mehandzhiyski, I. Zozoulenko, *ACS Appl. Energy Mater.* **2019**, *2*, 3568.
[87] D. Li, X. Sun, M. A. Khaleel, *J. Eng. Mater. Technol.* **2012**, *134*, 010911.
[88] F. Naddeo, L. Baldino, S. Cardea, A. Naddeo, E. Reverchon, *J. Supercrit. Fluids* **2018**, *140*, 248.
[89] J. Huang, D. Rodrigue, *Polym. Compos.* **2016**, *37*, 1180.
[90] H. Mohammadi, D. Boughner, L. E. Millon, W. K. Wan, *Proc. Inst. Mech. Eng. H* **2009**, *223*, 697.
[91] J. Li, Y. Li, Z. Li, Y. Wang, J. Jiang, *Wood Sci. Technol.* **2024**, *58*, 1971.
[92] N. Khan, N. Z. Zaragoza, C. E. Travis, M. Goswami, B. K. Brettmann, *ACS Omega* **2020**, *5*, 17129.
[93] M. Asgarpour Khansary, P. Pouresmaeel-Selakjani, M. A. Aroon, A. Hallajisani, J. Cookman, S. Shirazian, *Heliyon* **2020**, *6*, e05776.
[94] B. Mostofian, C. M. Cai, M. D. Smith, L. Petridis, X. Cheng, C. E. Wyman, J. C. Smith, *J. Am. Chem. Soc.* **2016**, *138*, 10869.
[95] M. D. Smith, X. Cheng, L. Petridis, B. Mostofian, J. C. Smith, *Sci. Rep.* **2017**, *7*, 14494.
[96] S. H. Liu, S. J. Rukmani, M. Mohan, Y. Yu, D. Vural, D. A. Johnson, K. Copenhaver, S. Bhagia, M. E. Lamm, K. Li, J. Chen, M. Goswami,

M. D. Smith, L. Petridis, S. Ozcan, J. C. Smith, *Proc. Natl. Acad. Sci. USA* **2024**, *121*, e2405107121.
[97] G. Liu, W. Li, L. Chen, X. Zhang, D. Niu, Y. Chen, S. Yuan, Y. Bei, Q. Zhu, *Colloids Surf. A Physicochem. Eng. Asp.* **2020**, *594*, 124663.
[98] V. Alizadeh, B. Kirchner, *J. Chem. Phys.* **2021**, *155*, 084501.
[99] M. Kostag, P. A. R. Pires, O. A. El Seoud, *Cellulose* **2020**, *27*, 3565.
[100] P. Posada, J. Velásquez-Cock, C. Gómez-Hoyos, A. M. Serpa Guerra, S. V. Lyulin, J. M. Kenny, P. Gañán, C. Castro, R. Zuluaga, *Cellulose* **2020**, *27*, 10649.
[101] H. Liu, K. L. Sale, B. M. Holmes, B. A. Simmons, S. Singh, *J. Phys. Chem. B* **2010**, *114*, 4293.
[102] H. Miyamoto, U. Schnupf, K. Ueda, C. Yamane, *Nord. Pulp Pap. Res. J.* **2015**, *30*, 67.
[103] B. Mostofian, J. C. Smith, X. Cheng, *Cellulose* **2014**, *21*, 983.
[104] S. H. Liu, S. J. Rukmani, M. Mohan, Y. Yu, D. Vural, D. A. Johnson, K. Copenhaver, S. Bhagia, M. E. Lamm, K. Li, J. Chen, M. Goswami, M. D. Smith, L. Petridis, S. Ozcan, J. C. Smith, *Proc. Natl. Acad. Sci. USA* **2024**, *121*, 2405107121.
[105] S. V. Pingali, M. D. Smith, S. H. Liu, T. B. Rawal, Y. Pu, R. Shah, B. R. Evans, V. S. Urban, B. H. Davison, C. M. Cai, A. J. Ragauskas, H. M. O'Neill, J. C. Smith, L. Petridis, *Proc. Natl. Acad. Sci. USA* **2020**, *117*, 16776.
[106] J. P. Wojeicchowski, A. M. Ferreira, T. Okura, M. Pinheiro Rolemberg, M. R. Mafra, J. A. P. Coutinho, *Ind. Eng. Chem. Res.* **2022**, *61*, 15631.
[107] Y. Zhao, J. Zhu, S. Wang, Y. Chang, W. Liu, *Physica B Condens. Matter* **2022**, *643*, 414178.
[108] M. Mohan, K. D. Jetti, S. Guggilam, M. D. Smith, M. K. Kidder, J. C. Smith, *ACS Sustainable Chem. Eng.* **2024**, *12*, 7040.
[109] R. Rahman, J. T. Foster, A. Haque, *J. Phys. Chem. A* **2013**, *117*, 5344.
[110] Q. Fan, X. Meng, Z. Li, G. Ma, Z. Wang, K. Zhang, C. He, D. Meng, *Constr. Build. Mater.* **2022**, *341*, 127879.
[111] Z. Wang, Z. Li, D. Chen, Z. Qin, L. Wang, X. Zhang, Z. Li, S. Lu, *Polym. Compos.* **2024**, *45*, 2841.
[112] Y. Mo, L. Yang, F. Yin, Y. Gao, R. Liao, *Polym. Compos.* **2022**, *43*, 1698.
[113] R. J. Moon, A. Martini, J. Nairn, J. Simonsen, J. Youngblood, *Chem. Soc. Rev.* **2011**, *40*, 3941.
[114] C. Sáenz Ezquerro, M. Laspalas, J. M. García Aznar, C. C Miñana, *Cellulose* **2023**, *30*, 705.
[115] W. Damm, A. Frontera, J. Tirado-Rives, W. L. Jorgensen, *J. Comput. Chem.* **1997**, *18*, 1955.
[116] J. H. McAliley, D. A. Bruce, *J. Chem. Theory Comput.* **2011**, *7*, 3756.
[117] W. Xia, X. Qin, Y. Zhang, R. Sinko, S. Keten, *Macromolecules* **2018**, *51*, 10304.
[118] D. M. Anstine, A. Strachan, C. M. Colina, *Modell. Simul. Mater. Sci. Eng.* **2020**, *28*, 025006.
[119] C. Park, J. Jung, G. J. Yun, *Compos. B Eng.* **2020**, *202*, 108439.
[120] M. Antlauf, N. Boulanger, L. Berglund, K. Oksman, O. Andersson, *Biomacromolecules* **2021**, *22*, 3800.
[121] K. Adachi, K. Daicho, M. Furuta, T. Shiga, T. Saito, T. Kodama, *Appl. Phys. Lett.* **2021**, *118*, 053701.
[122] W. Webo, L. M. Masu, P. K. Nziu, *Mater. Res. Express* **2022**, *9*, 035404.
[123] L. Mishnaevsky Jr, L. P. Mikkelsen, A. N. Gaduan, K. Y. Lee, B. Madsen, *Compos. Struct.* **2019**, *224*, 111024.
[124] D. Dhamodharan, V. Dhinakaran, P. N. P. Ghoderao, H. S. Byun, L. Wu, *Compos. B Eng.* **2022**, *238*, 109918.
[125] F. Naddeo, L. Baldino, S. Cardea, A. Naddeo, E. Reverchon, *Chem. Eng. Trans.* **2017**, *57*, 1513.
[126] S. Zhang, J. Liu, Q. Guo, N. Wei, Y. Ning, Y. Bai, Y. Tian, T. Wang, Z. Sun, Y. Pu, *Compos. Part A Appl. Sci. Manuf.* **2023**, *165*, 107329.
[127] X. Gao, E. Sozumert, Z. Shi, G. Yang, V. V. Silberschmidt, *Mater. Sci. Eng. C Mater. Biol. Appl.* **2017**, *77*, 9.
[128] H. Huang, X. Zhang, Z. Dong, X. Zhao, B. Guo, *J. Colloid Interface Sci.* **2022**, *625*, 817.
[129] J. Shojaeiarani, M. Hosseini-Farid, D. Bajwa, *Mech. Mater.* **2019**, *135*, 77.
[130] A. Shakil, S. Kim, A. A. Polycarpou, *Adv. Mater. Interfaces* **2022**, *9*, 2101640.
[131] K. Zhao, S. Li, M. Huang, X. Shi, G. Zheng, C. Liu, K. Dai, C. Shen, R. Yin, J. Z. Guo, *Chem. Eng. J.* **2019**, *358*, 924.
[132] T. Htira, S. Zid, M. Zinet, E. Espuche, *Polymers* **2021**, *13*, 2615.
[133] O. H. M. Almahmoud, *Design Optimization of Functionalized Silica-Polymer Nanocomposite through Finite Element and Molecular Dynamics Modeling*. Ph.D., University of North Texas, **2020**.
[134] S. De, B. James, J. Ji, S. Wasti, S. Zhang, S. Kore, H. Tekinalp, Y. Li, E. E. Ureña-Benavides, U. Vaidya, A. J. Ragauskas, E. Webb, S. Ozcan, X. Zhao, In *Advances in Bioenergy*, (Eds.: Y. Li, C. Chang), Elsevier, Amsterdam, Netherlands, **2023**, pp. 145–196.
[135] K. Lin, Z. Wang, *Commun. Mater.* **2023**, *4*, 66.
[136] D. J. Gardner, J. Anderson, H. Tekinalp, P. S. S. Ozcan in *International Forest Products Congress* (Eds: I. Aydin, E. D. G.), Karadeniz Technical University, Karadeniz Technical University Faculty of Forestry, Department of Forest Industry Engineering, 61080 Trabzon /Turkey, **2018**, pp. 13-22.
[137] H. W. Kim, M. W. Park, J. Y Lim, *Sci. Eng. Compos. Mater.* **2020**, *27*, 290.
[138] W. Xu, X. Wang, N. Sandler, S. Willför, C. Xu, *ACS Sustainable Chem. Eng.* **2018**, *6*, 5663.
[139] A. Ji, S. Zhang, S. Bhagia, C. G. Yoo, A. J. Ragauskas, *RSC Adv.* **2020**, *10*, 21698.
[140] S. Zhang, X. Meng, S. Bhagia, A. Ji, M. D Smith, Y. Y. Wang, B. Liu, C. G. Yoo, D. P. Harper, A. J. Ragauskas, *Chem. Eng. J.* **2024**, *481*, 148449.
[141] M. K. Hausmann, G. Siqueira, R. Libanori, D. Kokkinis, A. Neels, T. Zimmermann, A. R. Studart, *Adv. Funct. Mater.* **2020**, *30*, 1904127.
[142] V. C. F. Li, C. K. Dunn, Z. Zhang, Y. Deng, H. J. Qi, *Sci. Rep.* **2017**, *7*, 8018.
[143] M. K. Hausmann, P. A. Rühs, G. Siqueira, J. Läuger, R. Libanori, T. Zimmermann, A. R. Studart, *ACS Nano* **2018**, *12*, 6926.
[144] K. Markstedt, A. Escalante, G. Toriz, P. Gatenholm, *ACS Appl. Mater. Interfaces* **2017**, *9*, 40878.
[145] C. Qian, L. Li, M. Gao, H. Yang, Z. Cai, B. Chen, Z. Xiang, Z. Zhang, Y. Song, *Nano Energy* **2019**, *63*, 103885.
[146] J. Wang, A. Chiappone, I. Roppolo, F. Shao, E. Fantino, M. Lorusso, D. Rentsch, K. Dietliker, C. F. Pirri, H. Grützmacher, *Angew. Chem. Weinheim Bergstr. Ger.* **2018**, *130*, 2377.
[147] D. Kam, M. Chasnitsky, C. Nowogrodski, I. Braslavsky, T. Abitbol, S. Magdassi, O. Shoseyov, *Colloids Interfaces* **2019**, *3*, 46.
[148] W. Wu, A. DeConinck, J. A. Lewis, *Adv. Mater.* **2011**, *23*, H178.
[149] S. Zhang, M. Li, N. Hao, A. J. Ragauskas, *ACS Omega* **2019**, *4*, 20197.
[150] S. Zhang, S. Bhagia, M. Li, X. Meng, A. J. Ragauskas, *Mater. Des.* **2021**, *206*, 109773.
[151] J. Sutton, K. Rajan, D. P. Harper, S. C. Chmely, *ACS Appl. Mater. Interfaces* **2018**, *10*, 36456.
[152] E. F. Douglass, H. Avci, R. Boy, O. J. Rojas, R. Kotek, *Polym. Rev.* **2018**, *58*, 102.
[153] H. Kargarzadeh, M. Mariano, J. Huang, N. Lin, I. Ahmad, A. Dufresne, S. Thomas, *Polymer* **2017**, *132*, 368.
[154] S. M. El Awad Azrak, C. M. Clarkson, R. J. Moon, G. T. Schueneman, J. P. Youngblood, *ACS Appl. Polym. Mater.* **2019**, *1*, 2525.
[155] S. M. El Awad Azrak, W. J. Costakis, R. J. Moon, G. T. Schueneman, J. P. Youngblood, *ACS Appl. Polym. Mater.* **2020**, *2*, 3365.
[156] Q. F. Guan, H. B. Yang, Z. M. Han, L. C. Zhou, Y. B. Zhu, Z. C. Ling, H. B. Jiang, P. F. Wang, T. Ma, H. A. Wu, S. H. Yu, *Sci. Adv.* **2020**, *6*, eaaz1114.
[157] X. Han, Y. Ye, F. Lam, J. Pu, F. Jiang, *J. Mater. Chem. A Mater. Energy Sustain.* **2019**, *7*, 27023.

[158] C. M. Clarkson, S. M. El Awad Azrak, E. S. Forti, G. T. Schueneman, R. J. Moon, J. P. Youngblood, *Adv. Mater.* **2021**, *33*, 2000718.
[159] K. Li, C. M. Clarkson, L. Wang, Y. Liu, M. Lamm, Z. Pang, Y. Zhou, J. Qian, M. Tajvidi, D. J. Gardner, H. Tekinalp, L. Hu, T. Li, A. J. Ragauskas, J. P. Youngblood, S. Ozcan, *ACS Nano* **2021**, *15*, 3646.
[160] Architects, S. Flotsam & Jetsam, https://www.shoparc.com/projects/design-miami/, (accessed: June 2024).
[161] J. Jiang, H. Oguzlu, F. Jiang, *Chem. Eng. J.* **2021**, *405*, 126668.
[162] BioHome3D – Advanced Structures & Composites Center – University of Maine, https://composites.umaine.edu/biohome3d/ (aceessed: June 2024).
[163] H. Tekinalp, D. Ker, X. Zhao, B. Benson, M. Buziak, V. Kunc, W. Peter, S. Ozcan, in CAMX 2019, NA SAMPE, **2019**.
[164] Q. Wang, C. Ji, L. Sun, J. Sun, J. Liu, *Molecules* **2020**, *25*, 2319.
[165] L. Wang, D. J. Gardner, D. W. Bousfield, *Polym. Eng. Sci.* **2018**, *58*, 793.
[166] C. M. Clarkson, S. M. El Awad Azrak, G. T. Schueneman, J. F. Snyder, J. P. Youngblood, *Polymer* **2020**, *187*, 122101.
[167] K. Shi, G. Liu, H. Sun, B. Yang, Y. Weng, *Polymers* **2022**, *14*, 4305.
[168] A. Gupta, W. Simmons, G. T. Schueneman, E. A. Mintz, *J. Therm. Anal. Calorim.* **2016**, *126*, 1243.
[169] L. Wang, W. Gramlich, D. Gardner, Y. Han, M. Tajvidi, *J. Compos. Sci.* **2018**, *2*, 7.
[170] T. Ambone, A. Torris, K. Shanmuganathan, *Polym. Eng. Sci.* **2020**, *60*, 1842.
[171] H. L. Tekinalp, X. Meng, Y. Lu, V. Kunc, L. J. Love, W. H. Peter, S. Ozcan, *Compos. B Eng.* **2019**, *173*, 106817.
[172] M. Latif, Y. Jiang, B. Kumar, J. M. Song, H. C. Cho, J. Kim, *Adv. Mater. Interfaces* **2022**, *9*, 2200280.
[173] V. Klar, J. Pere, T. Turpeinen, P. Kärki, H. Orelma, P. Kuosmanen, *Sci. Rep.* **2019**, *9*, 3822.
[174] K. De France, Z. Zeng, T. Wu, G. Nyström, *Adv. Mater.* **2021**, *33*, 2000657.
[175] A. Barkane, E. Kampe, O. Platnieks, S. Gaidukovs, *Nanomaterials* **2021**, *11*, 1791.
[176] W. Zhou, Z. Wu, F. Xie, S. Tang, J. Fang, X. Wang, *Carbohydr. Polym.* **2021**, *273*, 118545.
[177] M. Lille, A. Nurmela, E. Nordlund, S. Metsä-Kortelainen, N. Sozer, *J. Food Eng.* **2018**, *220*, 20.
[178] O. E. Adedeji, J. Y. Choi, G. E. Park, H. J. Kang, M. O. Aminu, J. H. Min, C. E. Chinma, K. D. Moon, Y. H. Jung, *Innov. Food Sci. Emerg. Technol.* **2022**, *80*, 103086.
[179] S. M. Amin Ojagh, M. Amini, S. Cranmer-Smith, F. Vahabzadeh, M. Arjmand, K. C. Tam, O. J. Rojas, M. Kamkar, T. G. M. van de Ven, *ACS Sustainable Chem. Eng.* **2023**, *11*, 5674.
[180] H. P. Voisin, K. Gordeyeva, G. Siqueira, M. K. Hausmann, A. R. Studart, L. Bergström, *ACS Sustainable Chem. Eng.* **2018**, *6*, 17160.
[181] Y. Li, H. Zhu, Y. Wang, U. Ray, S. Zhu, J. Dai, C. Chen, K. Fu, S. H. Jang, D. Henderson, T. Li, L. Hu, *Small Methods* **2017**, *1*, 1700222.
[182] K. M. O. Håkansson, I. C. Henriksson, C. de la Peña Vázquez, V. Kuzmenko, K. Markstedt, P. Enoksson, P. Gatenholm, *Adv. Mater. Technol.* **2016**, *1*, 1600096.
[183] Q. Wang, X. Liu, Z. Qiang, Z. Hu, X. Cui, H. Wei, J. Hu, Y. Xia, S. Huang, J. Zhang, K. Fu, Y. Chen, *Compos. Sci. Technol.* **2022**, *227*, 109601.
[184] Y. Shao, D. Chaussy, P. Grosseau, D. Beneventi, *Ind. Eng. Chem. Res.* **2015**, *54*, 10575.
[185] Y. Chen, Z. Yu, Y. Ye, Y. Zhang, G. Li, F. Jiang, *ACS Nano* **2021**, *15*, 1869.
[186] H. Lee, S. Kim, S. Shin, J. Hyun, *Carbohydr. Polym.* **2021**, *253*, 117238.
[187] S. Shin, J. Hyun, *ACS Appl. Mater. Interfaces* **2017**, *9*, 26438.
[188] A. Saddique, I. W. Cheong, *Korean J. Chem. Eng.* **2021**, *38*, 2171.
[189] L. Huang, X. Du, S. Fan, G. Yang, H. Shao, D. Li, C. Cao, Y. Zhu, M. Zhu, Y. Zhang, *Carbohydr. Polym.* **2019**, *221*, 146.
[190] S. D. Dutta, J. Hexiu, D. K. Patel, K. Ganguly, K. T. Lim, *Int. J. Biol. Macromol.* **2021**, *167*, 644.
[191] S. Sultan, A. P. Mathew, *J. Vis. Exp.* **2019**, *146*, 59401.
[192] Y. Jiang, J. Zhou, H. Shi, G. Zhao, Q. Zhang, C. Feng, X. Xv, *J. Mater. Sci.* **2020**, *55*, 2618.
[193] J. Wei, B. Wang, Z. Li, Z. Wu, M. Zhang, N. Sheng, Q. Liang, H. Wang, S. Chen, *Carbohydr. Polym.* **2020**, *238*, 116207.
[194] A. M. Cakmak, S. Unal, A. Sahin, F. N. Oktar, M. Sengor, N. Ekren, O. Gunduz, D. M. Kalaskar, *Polymers* **2020**, *12*, 1962.
[195] S. Sultan, A. P. Mathew, *Nanoscale* **2018**, *10*, 4421.
[196] W. Xu, B. Z. Molino, F. Cheng, P. J. Molino, Z. Yue, D. Su, X. Wang, S. Willför, C. Xu, G. G. Wallace, *ACS Appl. Mater. Interfaces* **2019**, *11*, 8838.
[197] M. Fermani, V. Platania, R. M. Kavasi, C. Karavasili, P. Zgouro, D. Fatouros, M. Chatzinikolaidou, N. Bouropoulos, *Appl. Sci.* **2021**, *11*, 8677.
[198] N. Wattanaanek, S. Suttapreyasri, B. Samruajbenjakun, *J. Funct. Biomater.* **2022**, *13*.
[199] D. Nguyen, D. A. Hägg, A. Forsman, J. Ekholm, P. Nimkingratana, C. Brantsing, T. Kalogeropoulos, S. Zaunz, S. Concaro, M. Brittberg, A. Lindahl, P. Gatenholm, A. Enejder, S. Simonsson, *Sci. Rep.* **2017**, *7*, 658.
[200] Y. Wu, Y. Wang, F. Wang, Y. Huang, J. He, *Polymers* **2022**, *14*, 4756.
[201] O. C. Gunes, A. Kara, G. Baysan, R. Bugra Husemoglu, P. Akokay, A. Ziylan Albayrak, B. U. Ergur, H. Havitcioglu, *J. Biomater. Appl.* **2022**, *37*, 683.
[202] M. Leonovich, V. Korzhikov-Vlakh, A. Lavrentieva, I. Pepelanova, E. Korzhikova-Vlakh, T. Tennikova, *Polymers* **2023**, *15*, 651.
[203] D. Aki, S. Ulag, S. Unal, M. Sengor, N. Ekren, C. C. Lin, H. Yılmazer, C. B. Ustundag, D. M. Kalaskar, O. Gunduz, *Mater. Des.* **2020**, *196*, 109094.
[204] I. Averianov, M. Stepanova, O. Solomakha, I. Gofman, M. Serdobintsev, N. Blum, A. Kaftuirev, I. Baulin, J. Nashchekina, A. Lavrentieva, T. Vinogradova, V. Korzhikov-Vlakh, E. Korzhikova-Vlakh, *J. Biomed. Mater. Res. B Appl. Biomater.* **2022**, *110*, 2422.
[205] M. Ul-Islam, S. Khan, M. W. Ullah, J. K. Park, *Biotechnol. J.* **2015**, *10*, 1847.
[206] H. G. de Oliveira Barud, R. R. da Silva, H. da Silva Barud, A. Tercjak, J. Gutierrez, W. R. Lustri, O. B. de Oliveira Junior, S. J. L. Ribeiro, *Carbohydr. Polym.* **2016**, *153*, 406.
[207] L. Diaz-Gomez, I. Gonzalez-Prada, R. Millan, A. Da Silva-Candal, A. Bugallo-Casal, F. Campos, A. Concheiro, C. Alvarez-Lorenzo, *Carbohydr. Polym.* **2022**, *278*, 118924.
[208] J. Vadillo, I. Larraza, T. Calvo-Correas, L. Martin, C. Derail, A. Eceiza, *Polymers* **2022**, *14*, 4999.
[209] K. Markstedt, A. Mantas, I. Tournier, H. Martínez Ávila, D. Hägg, P. Gatenholm, *Biomacromolecules* **2015**, *16*, 1489.
[210] G. Melilli, I. Carmagnola, C. Tonda-Turo, F. Pirri, G. Ciardelli, M. Sangermano, M. Hakkarainen, A. Chiappone, *Polymers* **2020**, 1655.
[211] J. Guo, Q. Li, R. Zhang, B. Li, J. Zhang, L. Yao, Z. Lin, L. Zhang, X. Cao, B. Duan, *Biomacromolecules* **2022**, *23*, 877.
[212] M. Babi, R. Riesco, L. Boyer, A. Fatona, A. Accardo, L. Malaquin, J. Moran-Mirabal, *ACS Appl. Bio Mater.* **2021**, *4*, 8443.
[213] M. J. Sawkins, P. Mistry, B. N. Brown, K. M. Shakesheff, L. J. Bonassar, J. Yang, *Biofabrication* **2015**, *7*, 035004.
[214] S. Kim, H. Baid, A. Hassen, A. Kumar, J. Lindahl, D. Hoskins, C. Ajinjeru, C. Duty, P. Yeole, U. Vaidya, R. Dinwiddie, F. Abdi, L. Love, S. Simunovic, V. Kunc, in *CAMX 2019, NA SAMPE*, **2019**.
[215] A. A. Hassen, R. B. Dinwiddie, S. Kim, H. L. Tekinalp, V. Kumar, J. Lindahl, P. Yeole, C. Duty, U. Vaidya, H. Wang, V. Kunc, *Polym. Compos.* **2022**, *43*, 3678.
[216] L. Liu, E. Jo, D. Hoskins, U. Vaidya, S. Ozcan, F. Ju, S. Kim, *Addit. Manuf.* **2023**, *72*, 103597.
[217] M. Ishii, T. Ito, H. Sado, I. Kuwajima, *Sci. Technol. Adv. Mater.: Meth.* **2024**, *4*, 2354649.

Shuvodeep De is a faculty member at Texas State University with a research focus on advanced computational and materials engineering. Prior to his current role, he was part of the Multiscale Materials Group at Oak Ridge National Laboratory within the Computational Sciences and Engineering Division. He received his Ph.D. from Virginia Tech, specializing in structural and aeroelastic optimization. Dr. De's research interests encompass additive manufacturing, nano-composites, hyper-elastic materials, finite element simulations, scientific workflows, general-purpose GPU computation, and physics-informed machine learning. His work integrates computational techniques with advanced materials research, contributing to the development of innovative solutions in engineering and manufacturing.

Shalini J. Rukmani is a postdoctoral research associate in the computational molecular biophysics group at the University of Tennessee/Oak Ridge National Laboratory. Her research focus is on understanding structure-property relationships through molecular simulations in synthetic and bio-based polymers for diverse applications including gas separation membranes, drug delivery systems, renewable energy, and upcycled plastics. Her current work focuses on computationally designing additive-manufactured high-performance thermoplastic nanocomposites and rational drug design for infectious diseases.

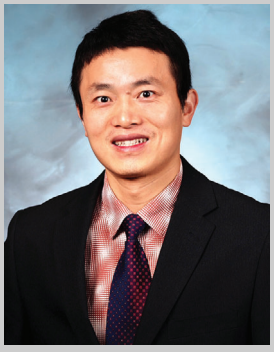

Xianhui Zhao is an R&D Staff member of Oak Ridge National Laboratory. He received a PhD in Agricultural, Biosystems, and Mechanical Engineering. To improve the feedstock value and reduce the environmental impacts, his research interests and expertise fall in bio-based materials. These materials include biomass natural fiber polymer composite, biofuel, biochar, biogas, etc. The tools he has used or developed include manufacturing (3D printing, compression molding, injection molding, extrusion), pyrolysis reactor, hydrodeoxygenation reactor, biogas reforming reactor, and Fischer–Tropsch synthesis reactor.

Samarthya Bhagia is a former staff member of ORNL. He is known for his works in the process engineering of biofuels from lignocellulosic feedstocks, structural characterization of lignin, chemistry of carbohydrate polymers, and high-resolution imaging of biological structures. He has specialization in NMR spectroscopy of macromolecules and extensive experience in the characterization of thermoplastics and manufacturing of bio-based composites. He currently serves as the senior scientist at PlantSwitch Inc. where he develops bio-derived home compostable materials for the food packaging industry.

Monojoy Goswami is an R&D staff member at ORNL's Chemical Sciences Division. Dr. Goswami did PhD in theoretical physics and currently focuses on interdisciplinary research in soft condensed matter physics. He is an expert in large-scale molecular dynamics (MD) simulations of soft matter. He published >50 journal papers, 2 patents, and gave ≈40 presentations. His research in large-scale simulation of polymer nanocomposites, charged polymer, polymer batteries, polymeric solar cells and structural and dynamical response of biopolymers have been widely cited. He is a regular user of Frontier supercomputer and an expert in high-performance computing.

Sana Elyas is responsible for evaluating and aligning industry partners with core research activities at the Manufacturing Demonstration Facility (MDF) at Oak Ridge National Laboratory (ORNL). She develops technical collaborations addressing industry challenges, directly aligning with Department of Energy (DOE) initiatives in additive manufacturing, composites, bio-based materials, and clean energy technology. With over 12 years of experience leading global projects and working with diverse teams, she advances markets and new product applications through innovative materials and manufacturing processes. She holds a bachelor's in aeronautical engineering and a master's in aerospace engineering, with expertise in composite materials and manufacturing processes.

Wei Zhao is an Assistant Professor in the Mechanical and Aerospace Engineering Department at Oklahoma State University, Stillwater, OK. He earned his Ph.D. in Aerospace Engineering from Virginia Tech. Dr. Zhao's research focuses on aerospace structures and materials, with a particular emphasis on their application in environmentally sustainable aircraft design. He is a recipient of the prestigious AIAA Abe Zarem Educator Award and the AIAA Structures Best Paper Award.

Jeremy C Smith is Governors Chair for Molecular Biophysics at the University of Tennessee/Oak Ridge National Laboratory. Smith has performed and directed research in a wide variety of fields, ranging from physics and chemistry to practical areas such as renewable energy, environmental science, and medicine. As of 2024, Smith had published over 500 peer-reviewed scientific articles.

Art Ragauskas held the first Fulbright Chair in Alternative Energy and is a Fellow of the American Association for the Advancement of Science, the International Academy of Wood Science, and TAPPI. In 2014, he assumed a Governor's Chair for Biorefining at the University of Tennessee's Department of Chemical and Biomolecular Engineering, with a complementary appointment in the UT Institute of Agriculture's Department of Forestry, Wildlife, and Fisheries and serves in the Energy and Environmental Sciences Directorate, Biosciences Division, at ORNL. His research program is directed at understanding and leveraging sustainable bioresources for the circular economy.

Ximin He is an associate professor of Materials Science and Engineering at the University of California, Los Angeles (UCLA) and the Faculty of California Nanosystems Institute (CNSI). Dr. He was a postdoctoral research fellow in the School of Engineering and Applied Science and the Wyss Institute of Bioinspired Engineering at Harvard University. Dr. He received her PhD in Chemistry at Melville Laboratory for Polymer Synthesis from the University of Cambridge. Dr. He's research focuses on bioinspired soft materials, structural polymers, and their physical, mechanical, electrical, and photothermal properties with broad applications in biomedicine, energy, environment, and robotics. Dr. He is the recipient of the NSF CAREER award, AFOSR Young Investigator award, Moore Inventor Fellow, CIFAR Global Scholar, SES Young Investigator Medal, International Society of Bionic Engineering (ISBE) Outstanding Youth Award, Advanced Materials Rising Star Award, 3M Non-tenured Faculty Award, and Hellman Fellows Award. Her research on bioinspired tough hydrogels, phototropic, phototaxic, homeostatic, and anti-icing materials have garnered a number of regional and international awards and was featured in >100 international news outlets.